

Copyright © 1995, by the author(s).
All rights reserved.

Permission to make digital or hard copies of all or part of this work for personal or classroom use is granted without fee provided that copies are not made or distributed for profit or commercial advantage and that copies bear this notice and the full citation on the first page. To copy otherwise, to republish, to post on servers or to redistribute to lists, requires prior specific permission.

**IMPEDANCE MODELING OF Cl_2/He
PLASMA DISCHARGES**

by

Antonio Jenaro Miranda

Memorandum No. UCB/ERL M95/31

27 April 1995

**IMPEDANCE MODELING OF Cl_2He
PLASMA DISCHARGES**

by

Antonio Jenaro Miranda

Memorandum No. UCB/ERL M95/31

27 April 1995

ELECTRONICS RESEARCH LABORATORY

College of Engineering
University of California, Berkeley
94720

Table of Contents

Chapter 1	Introduction	1
1.1	Motivation	1
1.2	Background	2
1.3	Thesis Organization	4
Chapter 2	Plasma Equipment and RF Sensor	5
2.1	Introduction	5
2.2	Lam Rainbow 4400	5
2.3	RF Sensor	6
Chapter 3	Impedance Models	9
3.1	Introduction	9
3.2	Bulk Region	11
3.3	Sheath Region	13
3.3.1	Electrons	13
3.3.2	Ions	14
3.4	Effects of Stray Impedances	15
3.5	Proposed Impedance Models	15
3.6	Conclusions	16
Chapter 4	Effects of Input Parameters	17
4.1	Introduction	17
4.2	The effect of RF Power	18
4.2.1	Bulk Resistance	18
4.2.2	Components of the Sheath Impedance	19
4.3	The effect of Chamber Pressure	20
4.3.1	Bulk Resistance	20
4.3.2	Components of the Sheath Impedance	21
4.4	Conclusions	22
Chapter 5	Experimental Design	23
5.1	Introduction	23
5.2	Initial Experiment	23
5.2.1	Test Structure	24
5.2.2	Experimental Design	24
5.2.2.1	The Extended Phase	26
5.2.2.2	The Diagnosis Phase	27

5.3	Verification Experiment	28
5.3.1	Test Structure	29
5.3.2	Verification Experimental Design	29
5.4	Stray Impedance Characterization	33
5.4.1	Stray Capacitance Network	34
5.4.2	Two-Port Stray Network	35
5.5	Conclusions	37
Chapter 6	Results	38
6.1	Introduction	38
6.2	Initial experiment	39
6.3	Verification Experiment	44
6.3.1	Impedance Models with no Stray Impedance Network	45
6.3.1.1	Real Impedance	45
6.3.1.2	Imaginary Impedance	52
6.3.1.3	Conclusions for Impedance Models with no Stray Impedance	54
6.3.2	Impedance Models with Stray Capacitance	55
6.3.3	Impedance Models with Two-Port Stray Networks	59
6.3.4	Power-Pressure Interactions	63
6.3.4.1	Real Impedance	64
6.3.4.2	Imaginary Impedance	65
6.3.4.3	Results	65
6.3.5	Conclusions from the Verification Experiment	67
Chapter 7	Conclusions	69
	References	71
Appendix A	Modifications to the Real Power Monitor Software	74
Appendix B	Test Structure Process Steps for the Experiments	77

List of Figures

Figure 2.1	The Comdel monitoring system and the various components which contribute to power losses in a parallel plate reactor.	8
Figure 3.1	Typical (a) discharge impedance models, and (b) networks used to represent the stray impedances in plasma etch systems.	10
Figure 3.2	Schematic of the plasma discharge and chamber, with the different regions annotated.	12
Figure 3.3	Proposed models to characterize the Cl_2/He plasma discharge.	16
Figure 5.1	Test structure for the Initial Experiment.	24
Figure 5.2	Depiction of three input settings for the (a) Fractional Factorial Phase (not used), (b) the Extended, and (c) the Diagnosis phase experiments..	26
Figure 5.3	Test structure for the Verification Experiment.	29
Figure 5.4	Plasma etch system with the stray capacitances annotated..	35
Figure 5.5	Stray embedded network as it relates to the plasma etch system in the Berkeley Microfabrication Laboratory.	36
Figure 6.1	Real Impedance versus the Inverse of Current Density for the Extended and Diagnosis phase.	40
Figure 6.2	Real Impedance plotted versus the input parameters using Extended phase data: (a) Z_{real} vs. Pressure, (b) Z_{real} vs. Gap separation, (c) Z_{real} vs. Gas ratio, and (d) Z_{real} vs. Total Flow.....	41
Figure 6.3	Imaginary Impedance versus (a) RF Power and (b) Pressure for the Extended phase.	42
Figure 6.4	Impedance models of the Cl_2/He discharge. (a) with no sheath resistance, and (b) with the sheath resistance included..	45
Figure 6.5	Current density as a function of (a) RF power and (b) pressure.....	46
Figure 6.6	Absorbed power versus RF input power.....	46

Figure 6.7	Z_{real} versus $1/J_{\text{eb}}$ for RF power varying only. The results are for a linear fit.....	48
Figure 6.8	The (a) rms voltage, (b) dc bias potential and (c) sheath potential, as a function of the RF power.....	50
Figure 6.9	Z_{real} as a function of $1/J_{\text{eb}}$ taking into account the sheath resistance. . . .	51
Figure 6.10	Real Impedance as a function of pressure.. . . .	52
Figure 6.11	Imaginary Impedance as a function of $1/J_{\text{eb}}$ for RF power varying only.	53
Figure 6.12	Imaginary impedance as a function of pressure.	54
Figure 6.13	Impedance models with a stray capacitance factor included, (a) without the sheath resistance, (b) with the sheath resistance.	55
Figure 6.14	Schematic of system with stray capacitance and different currents annotated.	56
Figure 6.15	Current Density as a function of (a) RF power, and (b) pressure. Stray capacitance is included in the impedance model.. . . .	57
Figure 6.16	Results for the (a) real impedance and (b) imaginary impedance as a function of RF power. Stray capacitance is included in the impedance model.	58
Figure 6.17	Results for the (a) real impedance and (b) imaginary impedance as a function of pressure. Stray capacitance is included in the impedance model.	58
Figure 6.18	Impedance models with a two-port stray network included, (a) without the sheath resistance, (b) with the sheath resistance.	59
Figure 6.19	Two-port Network with RF and Plasma signals denoted.	60
Figure 6.20	Current density as a function of (a) RF power and (b) pressure. Two-port stray network included in the impedance model.. . . .	61
Figure 6.21	Real and Imaginary impedance as a function of RF power ($1/J_{\text{eb}}$). Two-port stray network included.	62
Figure 6.22	Real and Imaginary impedance as a function of pressure. Two-port stray network included.	62
Figure 6.23	Impedance Representation of a Cl_2/He discharge.	63
Figure 6.24	Z_{real} versus $1/J_{\text{eb}}$ power and pressure	65
Figure 6.25	Real impedance versus the inverse of current density for different pressure and RF power variations.....	67

List of Tables

Table 3.1	Operating Conditions	11
Table 5.1	Etch Recipes	25
Table 5.2	Change in Percent From Nominal	26
Table 5.3	Randomized Extended Phase Runs	27
Table 5.4	Randomized Diagnosis Phase Runs	28
Table 5.5	Verification Experiment: Input settings	30
Table 5.6	Ratio and Total Flows	30
Table 5.7	Pressure and Power settings for Interaction Terms	30
Table 5.8	Verification Experiment: Block I Randomized Runs	31
Table 5.9	Verification Experiment: Block II Randomized Runs	32
Table 5.10	Verification Experiment: Block III Randomized Runs	32
Table 5.11	Stray Impedance Measurements	33
Table 5.12	Parallel plate and Stray Capacitance	34
Table 5.13	Stray Impedance Parameters	37
Table 6.1	Impedance trends with input variations	43
Table 6.2	F-distributions for the Input Parameters	44
Table 6.3	Two-port Parameters	59
Table 6.4	Results for the Real Impedance with Multiple Effects	65
Table 6.5	Results for the Imaginary Impedance with Multiple Effects	66
Table 6.6	Summary of Extracted Relationships	67

List of Symbols

Symbol	Units	Description
A	m^2	Area of electrode
C_{parallel}	Farads	Parallel plate capacitance
C_{sh}	Farads	Sheath capacitance
$C_{\text{stray}}, C_{\text{st}}$	Farads	Stray capacitance
C_{system}	Farads	Plasma discharge capacitance, including the stray capacitance
d	m	Diameter of gas molecules
E	V/m	Electric Field
\tilde{I}	Amps	Phasor representation of RF current
I	Amps	RF current amplitude
I_{pl}	Amps	Plasma discharge current after correction for the stray impedance
I_{rms}	Amps	Root mean square current
I_{st}	Amps	Current through the stray capacitance
J_{eb}	Amps/ m^2	Electron current density
J_{i}	Amps/ m^2	Ion current density
j		imaginary number ($\sqrt{-1}$)
k	J/ $^{\circ}\text{K}$	Boltzmann's constant ($1.381 * 10^{-23}$)
l_{bulk}	m	Bulk thickness
l_{sh}	m	Sheath thickness
m_{e}	kg	Electron mass ($9.11 * 10^{-31}$)
m_{i}	kg	Ion mass
n_{e}	m^{-3}	electron density

Symbol	Units	Description
p	Pascal	Pressure
\tilde{P}	Watts	Phasor representation of absorbed power
P_{abs}	Watts	Absorbed power
q	C	Elementary charge ($1.602 * 10^{-19}$)
R_{bulk}	Ω	Bulk resistance
R_{sh}	Ω	Sheath resistance
T	$^{\circ}K$	Temperature
t	sec	Time
\tilde{V}	Volts	Phasor representation of RF voltage
V	Volts	RF voltage amplitude
V_{dc}	Volts	DC bias voltage
V_{elect}	Volts	Voltage at the top electrode
V_{pl}	Volts	Plasma discharge voltage after correction for the stray impedance
V_{rms}	Volts	Root mean square voltage
V_{sh}	Volts	Sheath voltage
ΔV_{bulk}	Volts	Change in bulk potential
\bar{v}	m/sec	Mean thermal velocity
\tilde{Z}	Ω	Phasor representation of impedance
Z_{imag}	Ω	Imaginary impedance
\hat{Z}_{imag}	Ω	Extracted value for the imaginary impedance
Z_m	Ω	Measured impedance
Z_{pl}	Ω	Plasma discharge impedance after correction for the stray impedance
Z_{real}	Ω	Real impedance of plasma discharge
\hat{Z}_{real}	Ω	Extracted value for the real impedance
Z_{sh}	Ω	Sheath impedance
Z_{11}	Ω	Two-port impedance parameter
Z_{12}	Ω	Two-port impedance parameter
Z_{21}	Ω	Two-port impedance parameter
Z_{22}	Ω	Two-port impedance parameter

Symbol	Units	Description
$ Z $	Ω	Determinant of the z-matrix
ϵ_0	F/m	Permittivity of vacuum ($8.854 * 10^{-12}$)
λ	m	Mean free path
μ_e	$m^2/V*sec$	Electron mobility
π		Pi (3.145)
θ	°	Phase shift
σ	$1/\Omega*m$	Conductivity
$\hat{\sigma}_{allpoints}^2$		Estimated variance of all data
$\hat{\sigma}_{centerpoints}^2$		Estimated variance of centerpoint data
ν_{eo}	1/sec	Electron-neutral collision frequency
ω	rad/sec	RF frequency ($8.52 * 10^7$)

Acknowledgments

I would like to express my sincere gratitude to my research advisor, Professor Costas J. Spanos, for his research guidance and support of my future goals. His sincerity and honest evaluation of my work were instrumental to my success here at Berkeley. I am also extremely grateful to Professor Michael Lieberman for his insightful suggestions during the review of this thesis.

The experiments discussed in this thesis were conducted in the Berkeley Microfabrication Laboratory. I am grateful to the entire staff, especially Debra and Dave Hebert, Maria Perez, Bob Hamilton, Evan Stateler, and Charlie Williams for sharing their respective expertise.

My experience at Berkeley would not have been as rewarding, if it were not for the support and interaction I had with the members of the BCAM group. I owe a debt of gratitude to Dr. Sherry Lee. Her knowledge and friendship helped me through many trying times, especially in the microlab. To all past and present BCAM members: Dr. Eric Boskin, Dr. Raymond Chen, Roawen Chen, Sean Cunningham, Zeina Daoud, Mark Hatzilambrou, Herb Huang, Anna Ison, Sovarong Leang, David Mudie, Xinhui Niu, David Rodriguez, Manolis Terrovitis, Mark Tian, Pamela Tsai and Crid Yu; I thank you for your constructive feedback and friendship.

I also wish to thank all my friends and the Starkweather family. Without you all, I never would have made it through graduate school. I extend a special thanks to my dearest friend, Royce Johnson. He has been my teacher, mentor, motivator and counselor ever since my days at Jefferson High School. I thank you.

Finally to my family, your support for my endeavors never wavered, even though my confidence often did. I live my life for you guys, and you are always in my heart and thoughts- LOS QUIERO.

This research has been sponsored by the Semiconductor Research Corporation (SRC), SEMATECH (93-MP-700, 94-YP-700), and California Micro with matching funds from Atmel Corporation, ABB, Hughes, National Semiconductor, Texas Instruments, Lam Research, and Advanced Micro Devices.

Chapter 1

Introduction

1.1 Motivation

With the advent of smaller feature sizes and the rising cost of semiconductor fabrication facilities, existing processing equipment must be utilized to its maximum capability, if the semiconductor industry is to remain competitive. One key piece of equipment in the fabrication process is the plasma etcher. With the dry etch potential for obtaining submicron dimensions, it becomes critical to better understand, monitor, and control this process step. This understanding may be garnered with the use of sensors. From optical emission spectroscopy [1][2] to Langmuir probes [3][4][5], the information collected from sensors is crucial in determining the effects of the plasma on the processing of different materials.

In particular, Radio Frequency (RF) or electrical sensors are important for several reasons. First, because they are non-intrusive, the information obtained in a research environment can be transferred directly to the manufacturing floor without affecting the process. Another important characteristic is that these sensors collect and report data in real time. This enables fast response time to any changes that occur during processing. RF monitors

also give information about the discharge which can be used to develop a physical understanding of the internal electrical characteristics of the plasma. At the very least, this information can be used to establish trends between the input settings and the electrical characteristics of the plasma source. However, much more can be drawn from this information.

Shifts in the electrical state of the plasma can be used to detect equipment malfunctions. This is accomplished by developing models which relate the input signals to the electrical signals. This information would be invaluable when performing diagnosis. For example, suppose the manometer becomes miscalibrated over the course of time. This will result in a shift of the chamber pressure from its set point. A corresponding shift in the electrical characteristics of the plasma discharge would then occur. By establishing an impedance model that is based on physical principles, this shift in impedance could be traced back to pressure changes.

1.2 Background

Electrical characterization of plasma discharges derives much of its understanding from earlier work performed on RF sputtering systems. Koenig and Maissel [6] and later, in more detail, Keller and Pennebaker [7] used equivalent circuit models to characterize the different mechanisms and regions in RF sputtering systems. The resulting work predicted the electrical characteristics of the RF sputtering systems under test.

These initial studies are the basis for much of the research done using impedance models to characterize plasma discharges. Impedance models have been used to varying levels of complexity depending on the focus of the research. In general, impedance models are used to physically explain the different mechanisms, which describe the plasma discharge under test. Many of the previous studies have concentrated on developing these physical relationships so as to better predict the internal characteristics of the plasma discharge [8]-[18]. Understanding how electron density, ion current density and electron temperature,

for example, vary under different operating conditions is a key in determining how to better control and diagnose plasma etching.

Additional detail is added to the equivalent impedance network by accounting for various secondary effects. The basic model used in several studies accounts only for the basic regions of the discharge. Other authors, however, went a step further and differentiated between electropositive and electronegative gas discharges [12]. The dominant ionic species that makeup an electropositive discharge, such as Argon, are very different from the makeup of SF_6 or Cl_2 - gas discharges, which are electronegative.

Another level of detail in impedance modeling, is to account for power losses throughout the plasma etch system [10][12][14][19]. The matching network, RF cables, and stray impedances in the chamber, may all contribute to power dissipation. Butterbaugh, Baston, & Sawin [14], among other authors have shown that anywhere between 10% and 90% of the input power is consumed outside the plasma discharge. Some studies try to account for some of these power losses by characterizing the stray impedances of the chamber. This network may be as simple as a stray capacitance or as complex as a two-port network. This two-port stray impedance is determined in a variety of ways, with one of the more popular ones being the de-embedding and unterminating method developed by Bauer and Penfield [20]. The characterization of the stray impedances adds another level of physical understanding to the plasma discharge system.

1.3 Thesis Organization

In this study, we attempt to use the vast existing knowledge of impedance modeling in order to characterize a Cl_2/He discharge. Using fundamental relationships to distinguish between different current transport mechanisms, an impedance model is developed. Functional dependencies are then established between the input variables and the impedance components. An experiment with varying RF power, pressure, and Cl_2 gas flow is performed on a Lam 4400 polysilicon etcher to verify these dependencies. The resulting

impedance model and the particular dependencies it describes can then be used for fault diagnosis.

An overview of the equipment and sensors used are provided in Chapter 2. Chapter 3 discusses the physical relationships used to arrive at the impedance model used to characterize our discharge. The relationships between the input parameters and the impedance network are discussed in Chapter 4. Chapter 5 reviews the experiments performed to analyze and verify the network, and Chapter 6 discusses the results. Finally, Chapter 7 summarizes the findings, and suggests the possible direction of future work in this area.

Chapter 2

Plasma Equipment and RF Sensor

2.1 Introduction

In this chapter the plasma equipment and the radio frequency (RF) sensor used for this study are reviewed. One of the objectives of this research is to make the results easily transferable to the manufacturing floor. In order to accomplish this task, the sensor must be non-intrusive and commercially available. Consequently, both the plasma etcher, as well as the RF sensor used in this experiment are commercially available items. Any methodology developed can therefore be incorporated into an existing production line, without fear of adversely affecting the final state of the wafer.

2.2 Lam Rainbow 4400

The system under investigation is the Lam Rainbow 4400 plasma etcher [21]. The Rainbow 4400 is a fully automated, single wafer plasma/RIE etching system. This parallel plate system controls the RF power, pressure, temperature, electrode gap and the flows of gases entering the chamber. During normal operation the chamber pressure is around 425

mtorr, and the wafer is transported via a load lock system. This helps to minimize any contaminants during the etch process. For better temperature control the wafer is clamped to the bottom electrode, which is cooled with Helium.

The gases used for this process are SF_6 for the pre-etch step and a mixture of Chlorine and Helium for the main etch step. The plasma is initiated with the application of a 13.56 MHz capacitively coupled power source. During operation, the process is monitored by several sensors that have been installed on the Rainbow 4400. These sensors include signals from the SECS-II (SEMI Equipment Communication Standard-II) monitor [22], an optical emission spectroscopy system [23], and the RF power monitor discussed below.

2.3 RF Sensor

The radio frequency (RF) sensor chosen to monitor the electrical characteristics of the Cl_2/He discharge is the Real Power Monitor (RPM-1) made by Comdel Inc. [24]. This commercial sensor has the benefit of being inexpensive and relatively non-intrusive. An additional feature, is that it can collect data at a rate of up to 10 samples per second, allowing for real time analysis of the data.

RPM-1 measures in real time the fundamental frequency waveforms of the RF current and voltage. The phasor representation of this data is then:

$$\tilde{V} = V e^{-j\omega t} \text{ (Volts)} \quad (2.1)$$

$$\tilde{I} = I e^{-j(\omega t + \theta)} \text{ (Amps)} \quad (2.2)$$

From the current and voltage waveforms (1) the rms voltage and current, (2) the real or forward power dissipated in the system, and (3) the impedance of the discharge is calculated. Due to the position of the real power monitor in the RF circuit, the value for the impedance also includes the stray impedances of the chamber. These parameters are defined as:

$$V_{\text{rms}} = \frac{V}{\sqrt{2}} \text{ (Volts)} \quad (2.3)$$

$$I_{\text{rms}} = \frac{I}{\sqrt{2}} \text{ (Amps)} \quad (2.4)$$

$$\text{Re}(\tilde{P}) = \text{Re}(\tilde{V} \cdot \tilde{I}) \text{ (Watts)} \quad (2.5)$$

$$\tilde{Z} = \frac{\tilde{V}}{\tilde{I}} = \frac{V}{I} e^{-j\theta} \text{ } (\Omega) \quad (2.6)$$

The data collected is manipulated via the RPM-1 processing unit. Accompanying software is used to display the information on a remote PC in our microfabrication facility. Modifications were made to the software in order to automate data collection for each individual wafer, and to transmit the resulting data files to a local area network of unix workstations. Modifications to the software code are included in Appendix A.

The RPM-1 is mounted on the top electrode as shown in Figure 2.1. This is done in order to eliminate the variabilities that are typically encountered when monitoring with a sensor situated at the RF generator or along the transmission line. These inconsistencies may include transmission line losses, matching network tuning window errors, and matching network losses [19]. Among others [10][12], Butterbaugh, Baston, and Sawin [14] have shown that the actual power dissipated in a plasma discharge maybe as low as 10% of the power produced from the RF generator. Most losses are attributed to the matching network and stray impedances, among other things. Therefore, judicious positioning of the RF sensor is critical for accurate measurements. The RPM-1 is reported to have an accuracy of 5% absolute, with a repeatability in the order of 3% to a phase angle of 85 degrees.

With the RF sensor in place, the electrical behavior of the plasma is monitored during operation. Comparative experiments done before nad after the installation of the RPM-1 sensor show little effect on the overall performance of the plasma etcher. The next step is to develop impedance relationships for the Cl_2/He discharge which describes its electrical behavior. This is discussed further in Chapter 3.

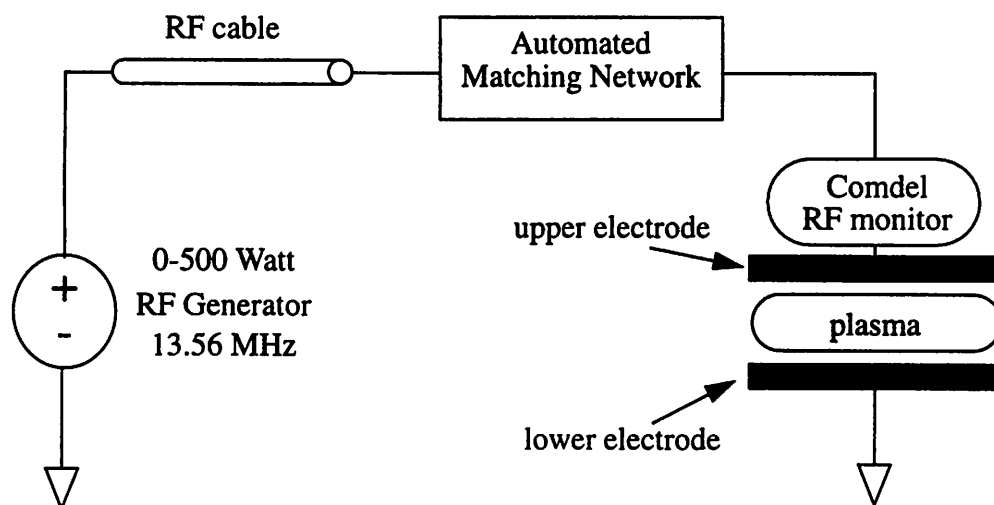


Figure 2.1 The Comdel monitoring system and the various components which contribute to power losses in a parallel plate reactor.

Chapter 3

Impedance Models

3.1 Introduction

A variety of impedance models have been used to describe the electrical behavior of the plasma discharge under investigation. The fundamental equivalent circuit tries to model the two major regions of the plasma, the bulk and sheath region. These circuits range from a simple series network of resistors and capacitors to a complex parallel/series network that account for second order effects. These effects include stray impedances in the system [7][9][12][13][14][17][18][20], and inductive effects in the bulk region [10][12]. Some of the more typical impedance and stray circuit models are illustrated in Figure 3.1.

The operating conditions of the plasma system will also have an effect on the impedance model chosen. Most of the impedance models used, try to account for changes in the operating conditions. These include the excitation frequency, the geometry of the chamber, the pressure and power ranges used, whether the RF source is DC or AC coupled, and the gases used for the etch process. Each one of these parameters may play a major or

minor role in the electrical characteristics of the Cl_2/He discharge. In most cases, the impedance model is verified using experiments or existing data from previous studies.

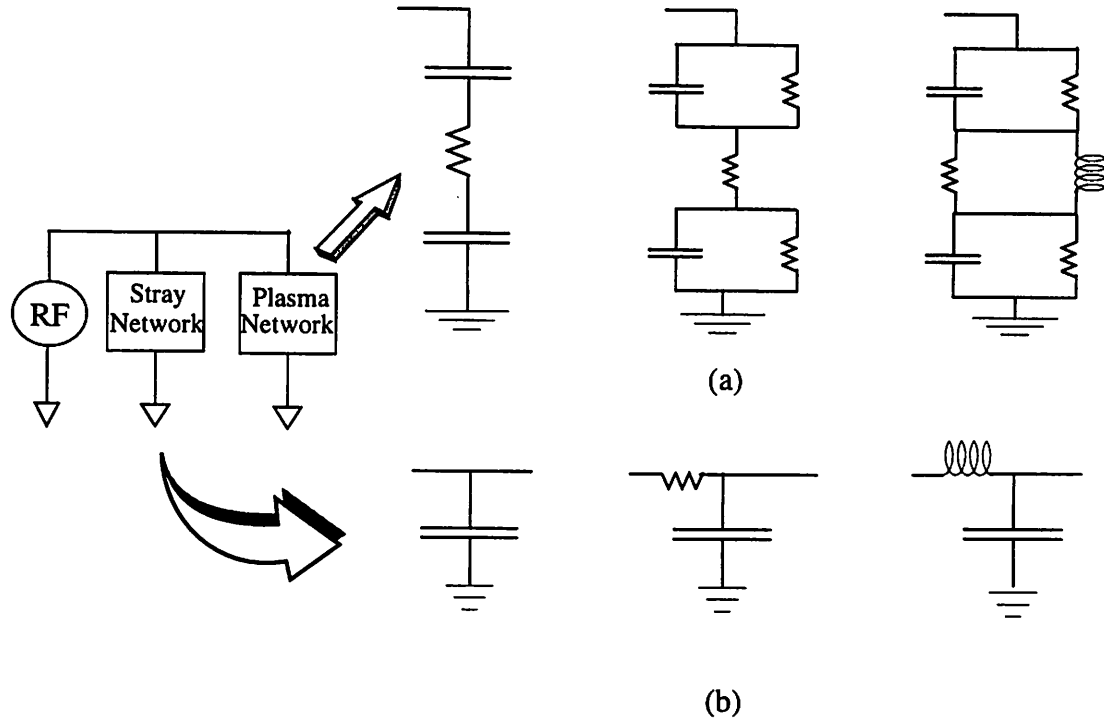


Figure 3.1 Typical (a) discharge impedance models, and (b) networks used to represent the stray impedances in plasma etch systems.

The objective of this chapter is to identify the major contributors to the electrical behavior of the Cl_2/He discharge under investigation. The standard operating conditions of our system are listed in Table 3.1. Two major regions, the bulk and the sheath are analyzed in some detail. The role of the stray impedance in the system is also investigated. Finally, several equivalent circuit models are proposed to characterize the plasma discharge under investigation. These impedance models are experimentally verified as described in Chapter 5.

Table 3.1 Operating Conditions

Parameter	Nominal Values ^a /Type
Frequency	13.56 Mhz
Coupling of RF source	AC capacitive
Power	204-316 W
Pressure	361-489 mTorr
Gas Flows: Cl ₂ He	136-184 sccm 360 sccm
Electrode Separation	0.9 cm

^a During our experiments, the values for RF power, pressure and Chlorine were changed about $\pm 15\%$ around the nominal values.

3.2 Bulk Region

There are two distinct regions in the plasma discharge shown in Figure 3.2. The first is commonly called the glow or bulk region. In this region the current mechanism is primarily described by the highly mobile electrons. This is because for a plasma operating at a frequency of 13.56 MHz, the dominant current-transport species are the electrons. As a result of the electron mobility being approximately one hundred times larger than the ion mobility, the electrons rapidly compensate for the changes in the bulk potential [8][25][26][27]. The current density in the bulk region can then be described by the flow of the mobility-limited electrons:

$$J_{eb} = \frac{q^2 n_e}{m_e} \cdot \left(\frac{v_{eo} - j\omega}{v_{eo}^2 + \omega^2} \right) \cdot E \quad (\text{Amps/m}^2) \quad (3.1)$$

or

$$J_{eb} \equiv \frac{q^2 n_e}{m_e v_{eo}} \cdot E \quad (\text{Amps/m}^2) \quad (3.2)$$

where q is the electron charge (C), n_e is the electron density (m^{-3}), m_e is the electron mass (kg), E is the electric field (V/m), v_{eo} is the electron-neutral collision frequency (sec^{-1}), and ω is the excitation frequency (rad/sec).

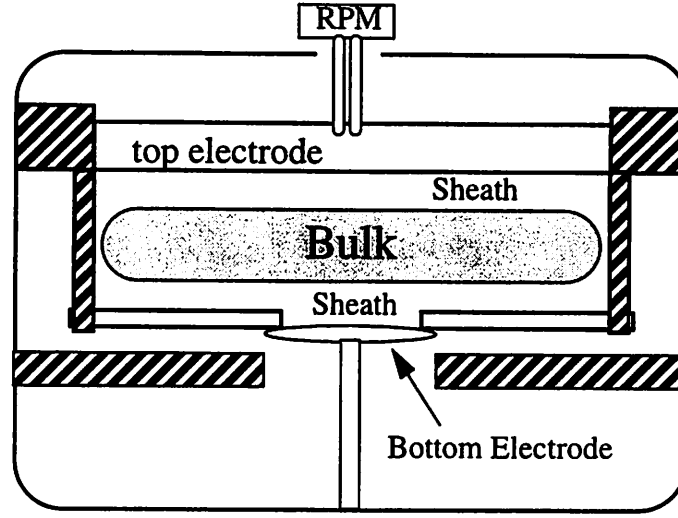


Figure 3.2 Schematic of the plasma discharge and chamber, with the different regions annotated.

Equation (3.2) is defined for operating conditions in which the electron-neutral collision frequency is much greater than the excitation frequency. The only time this is not true is when we are operating at very low pressures or at very high excitation frequencies. In those cases the inductive component of Eq (3.1) should also be considered. In our case, however, for pressures around 425 mtorr, ν_{e0} is much greater than the excitation frequency, ω .

The resistive losses due to the bulk region can be defined as:

$$R_{\text{bulk}} = \frac{\Delta V_{\text{bulk}}}{J_{\text{eb}} A} \quad (\Omega) \quad (3.3)$$

where A is the electrode area (m^2), and ΔV_{bulk} is the change in potential across the bulk region (volts). ΔV_{bulk} may also be defined in terms of the electric field:

$$\Delta V_{\text{bulk}} = E \cdot l_{\text{bulk}} \quad (\text{Volts}) \quad (3.4)$$

where l_{bulk} is the thickness of the bulk region (m). The bulk resistance is then found by substituting Eq (3.2) and (3.3) into (3.4):

$$R_{\text{bulk}} = \frac{l_{\text{bulk}} v_{\text{eo}} m_e}{q^2 n_e A} \quad (\Omega) \quad (3.5)$$

The mobility of electrons is approximated by [26]:

$$\mu_e \equiv \frac{q}{m_e v_{\text{eo}}} \quad (\text{m}^2/\text{V-sec}) \quad (3.6)$$

After substituting Eq (3.6) into the equation for the bulk resistance, Eq (3.5), becomes:

$$R_{\text{bulk}} = \frac{l_{\text{bulk}}}{q n_e A \mu_e} \quad (\Omega) \quad (3.7)$$

Thus, the bulk resistance as defined here, is inversely proportional to the mobility and density of electrons and proportional to the thickness of the bulk region.

3.3 Sheath Region

Two phenomena may play an important role in the current transport mechanisms of the sheath region. The first is the RF displacement current. The second is a dc current due to the flow of positive ions across the sheath.

3.3.1 Electrons

The large electric fields in the sheath repel electrons out of this region. The sheath, as a space charge region, is depleted of electrons and limits their flow to and from the bulk. As a first approximation, this phenomena may be modeled as a parallel-plate capacitor of the form:

$$C_{\text{sh}} = \frac{\epsilon_0 A}{l_{\text{sh}}} \quad (\text{Farads}) \quad (3.8)$$

where ϵ_0 is the permittivity of free space (F/m) and l_{sh} is the thickness of the sheath (m). Preliminary experimental data from Chlorine discharges show that this capacitor is an important circuit component.

3.3.2 Ions

Assuming the electron concentration in the sheath is minimal, the ion current density may be defined by the collisionless Child-Langmuir space-charge limited current [8][25]:

$$J_i = \frac{4\epsilon_o}{9} \cdot \left(\frac{2q}{m_i}\right)^{\frac{1}{2}} \left(\frac{V_{sh}^{\frac{3}{2}}}{l_{sh}^2}\right) \text{ (Amps/m}^2\text{)} \quad (3.9)$$

where J_i is the ion current density, m_i is the mass of the ions (kg), and V_{sh} is the potential drop across the sheaths (V). There maybe some concern that at our pressure (425mtorr) the ion current density in the sheath is governed by the collisional Child Langmuir law. Since the difference in the two equations is small, the effect on the current density should not be very significant. Thus, as a first approximation, the collisionless Child-Langmuir law is used to represent the ion current density. This phenomena may then be described as a nonlinear resistor of the form:

$$R_{sh} = \frac{V_{sh}}{J_i A} = \frac{9}{4A\epsilon_o} \cdot \left(\frac{m_i}{2qV_{sh}}\right)^{\frac{1}{2}} l_{sh}^2 \text{ } (\Omega) \quad (3.10)$$

This resistive component may be important in the circuit model if the ion current density in the sheath is substantial. This would be true when operating under high pressure (greater than 100 mtorr) or high power conditions [8]. The accuracy of the impedance model will depend on whether or not the nonlinear relationships between the experimental data and the sheath voltage and thickness exist, and how well these relationships can be modeled.

3.4 Effects of Stray Impedances

Many different models have been used to describe the stray impedances of a plasma etch system. These impedances include line inductances, stray capacitances between the powered electrode and the chamber, and resistive losses on the line. All these can contribute to inaccuracies in the electrical measurements of the true impedance in the chamber. In

the long run these effects may not prove detrimental to the validity of the models, but are included in order to explain discrepancies in measurements.

3.5 Proposed Impedance Models

The impedance models proposed for the characterization of the Cl_2/He discharge are enumerated in Figure 3.3. Six different models are proposed for experimental verification. Three of the impedance models include the effect of the sheath resistance (Figure 3.3 iv-vi), while the other three exclude this component (Figure 3.3 i-iii). The importance of the sheath resistance could not be ascertained from previous literature. This component is included in some of the impedance models to determine if it has a significant effect on the electrical signals of the plasma. Whether or not the sheath resistance is significant will depend on the amount of power dissipated in the sheath region. The discharge is also modeled with and without a stray impedance network as shown in Figure 3.3. Since Cl_2/He discharges are very capacitive, modeling the stray capacitance may prove useful in eliminating discrepancies in the impedance model. Two stray impedance networks are proposed to characterize the stray losses in our system: (1) a simple stray capacitor that shunts the plasma impedance (Figure 3.3 ii and v), and (2) a general two-port network to represent the stray impedance (Figure 3.3 iii and vi). The validity of these equivalent circuits will be examined in Chapter 6.

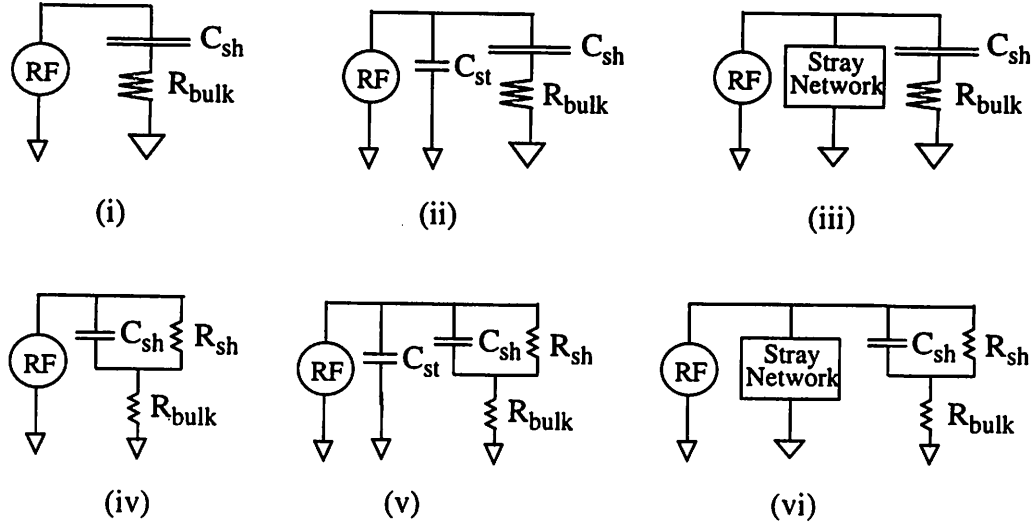


Figure 3.3 Proposed models to characterize the Cl_2/He plasma discharge.

3.6 Conclusions

The different transport mechanisms in both the sheath and bulk region were analyzed. Impedance models were developed that may prove useful in characterizing Cl_2/He discharges. Also, we investigated different forms of stray impedance networks in order to explain any discrepancies between the measured and theoretical models. To determine which one of the six models best characterizes the Cl_2/He discharge, experiments were designed and run. These experiments are discussed in Chapter 5. Before that, however, the next chapter investigates some of the relationships that may exist between the machine setting inputs (RF power and pressure) and the impedance models.

Chapter 4

Effects of Input Parameters

4.1 Introduction

With the framework of the impedance models in place, the next step is to determine the relationship between the input variables and the circuit components. Of particular interest is to determine how the sheath and bulk components vary with RF power and pressure. The relationships proposed are either derived from fundamental principles or are supported with experimental data.

Since the main concern is how the circuit parameters vary with the inputs close to the centerpoint settings (we explored a range of about $\pm 15\%$, as shown in Table 3.1), many of the relationships may not apply on a global scale. What looks linear over a small range of the input settings, may in fact be nonlinear, when observed over a large range. First order approximations are initially discussed, with additional detail included only if it is a major contributor to the impedance models.

4.2 The effect of RF Power

This section discusses some of the relationships between the circuit components and RF power. First, the resistance in the bulk region is analyzed. In section 4.3.2 the analysis focuses on the components in the sheath region and how they may vary with RF power.

4.2.1 Bulk Resistance

The real power absorbed in the system is a function of the real impedance and is defined as:

$$P_{abs} = \frac{1}{2} I^2 \cdot Z_{real} = \frac{1}{2} J_{eb}^2 \cdot \frac{Al_{bulk}}{\sigma} \text{ (Watts)} \quad (4.1)$$

where σ is the conductance of the bulk region ($1/\Omega\cdot m$), and all other parameters are defined as before. Since the bulk region is solely characterized by a resistive component, its effect on the total power dissipation in the system is significant. Actually, several studies have shown that the sheath resistance dissipates a maximum of 20% of the total power [12][14][17]. This of course will depend on the operating conditions, in particular the pressure range used. To determine a relationship between RF power and the bulk resistance, we assume that the actual power absorbed (P_{abs}) in the plasma discharge is a linear transformation of the RF power input. This assumption is verified experimentally in Chapter 6 (Figure 6.6).

Ulacia and McVittie [8] found the current density to be a linear function of RF power. If this is correct then from Eq (4.1) the conductivity will also increase linearly with RF power. The conductivity of a resistive material is defined as:

$$\sigma = q\mu_e n_e \quad (1/\Omega\cdot m) \quad (4.2)$$

The total dissipation for the system is then:

$$P_{abs} = J_{eb}^2 \cdot \frac{Al_{bulk}}{q\mu_e n_e} \text{ (Watts)} \quad (4.3)$$

The resistive component defined is of the same form as the bulk resistance defined in Eq (3.7). Therefore, if the major mode for power dissipation in the system is the bulk resistance, a direct relationship between RF power and bulk resistance is established.

A linear relationship thus exists between the product of electron mobility and density, and the power dissipated in the system. Variations in RF power will affect both the mobility and density of electrons in the bulk region. However, one further simplification proposed by McVittie and Ulacia [8] is that, for a given power range, the collision frequency is only weakly dependent on the power density. Since the collision frequency, as shown in Eq (3.6), is directly related to the electron mobility, a linear relationship exists between RF power and electron density.

4.2.2 Components of the Sheath Impedance

In this region the effect of RF power variations on the components is not as strong as in the bulk region. Recall from the full circuit impedance model that the sheath is represented by a capacitor and resistor in parallel. These equations are repeated below:

$$C_{sh} = \frac{\epsilon_0 A}{l_{sh}} \quad (\text{Farads}) \quad (4.4)$$

$$R_{sh} = \frac{9}{4A\epsilon_0} \cdot \left(\frac{m_i}{2qV_{sh}} \right)^{\frac{1}{2}} \cdot l_{sh}^2 \quad (\Omega) \quad (4.5)$$

The variables in Eqs (4.4) and (4.5) that could be affected by the RF power are the sheath thickness and voltage. The sheath voltage varies linearly with RF power. Empirically, this was verified using the experimental data from Chapter 6 (Figure 6.8). Since, from Eq (4.5), the sheath voltage has an inverse square root effect on the resistance, RF power should also have the same effect on the sheath resistance. The second parameter, sheath thickness, may also be affected by RF power. Aydil and Economou, however, show that for Chlorine discharges the sheath thickness and potential are weak functions of RF power at high pressures [11]. Whether or not RF power has a significant effect on the sheath components will be verified from the experiments performed. This is accomplished

by plotting the real impedance as a function of RF power. If the resulting plot is linear then we can conclude that the total resistance scales in a manner similar to the bulk resistance, as discussed in section 4.2.1.

4.3 The effect of Chamber Pressure

The major effects which dominate the relationship between pressure and the impedance model are discussed. In the bulk, we investigate how the electron mobility varies with pressure. In the sheath region a relationship between pressure and the sheath thickness is discussed.

4.3.1 Bulk Resistance

Referring to the formula for the bulk resistance in Eq (3.7), one of the major factors to account for, as pressure is varied, is the mobility of the electrons (μ_e). Several authors reference different experiments which show that the product of electron mobility and pressure is constant over a wide range of values [10][13][14][16][28]. This relationship is derived from the fundamental effect pressure has on the mean free path of particles. The mean free path of a gas molecule, is given by [29]:

$$\lambda = \frac{kT}{\sqrt{2}p\pi d^2} \quad (\text{m}) \quad (4.6)$$

where k is Boltzmann's constant ($\text{J}/^\circ\text{K}$), T is the temperature ($^\circ\text{K}$), p is the gas pressure (Pa), and d is the diameter of the gas molecules (m). The mean free path can then be related to the mobility of electrons with the following approximation [26]:

$$\mu_e \equiv \frac{q\lambda}{m_e \bar{v}} \quad (\text{m}^2/\text{V-sec}) \quad (4.7)$$

where \bar{v} is the mean thermal velocity (m/s). Substituting Eq (4.6) into (4.7) results in the inverse relationship between pressure and electron mobility referenced in the previous studies:

$$\mu_e = \frac{qkT}{m_e \bar{v} \sqrt{2p} \pi d^2} \quad (\text{m}^2/\text{V-sec}) \quad (4.8)$$

Both electron swarm experiments [14] and drift velocity data [28] have shown this linear relationship to exist.

4.3.2 Components of the Sheath Impedance

In the sheath region the capacitance, and to a lesser extent the sheath resistance are also affected by pressure variations. Several authors point out that a linear relationship between pressure and the imaginary impedance exist. This relationship stems from an inverse relationship between pressure and the sheath thickness [7]. The imaginary impedance for the full sheath circuit model is:

$$Z_{\text{imag}} = -\frac{2\omega C_{\text{sh}} R_{\text{sh}}^2}{1 + (\omega C_{\text{sh}} R_{\text{sh}})^2} \quad (\Omega) \quad (4.9)$$

Equation 4.9 can be rewritten with the full expressions for the sheath capacitance and resistance derived in Eq (3.8) and (3.10). After rearranging the terms, the imaginary impedance takes the following form:

$$Z_{\text{imag}} = -\frac{1}{\frac{\epsilon_0 A}{l_{\text{sh}}} \left(\frac{2qV_{\text{sh}}}{\left(\frac{9}{4}\right)^2 l_{\text{sh}}^2 m_i \omega} + \omega \right)} \quad (\Omega) \quad (4.10)$$

Now, if the sheath resistance is not a major component in this region, then the first term in the parenthesis of Eq (4.10) is negligible. The equation then simplifies to:

$$Z_{\text{imag}} \cong -\frac{l_{\text{sh}}}{\epsilon_0 A \omega} \quad (\Omega) \quad (4.11)$$

which is defined as the sheath capacitance. Therefore, a linear relationship between the imaginary impedance and the sheath thickness would indeed exist. This increase is a result of the inverse relationship between pressure and the mean free path. This relationship is examined in Chapter 6.

4.4 Conclusions

Expressions were proposed which relate the input parameters to the components of the impedance models. The focus of the analysis was on first order effects. When fundamental relationships were not used to relate the inputs to the impedance model, then experimental references were sited. The next chapter discusses the experiment designed and carried out in order to confirm these relationships.

Chapter 5

Experimental Design

5.1 Introduction

The relationships developed in Chapter 4 are confirmed with the experiments described in this chapter. The models proposed in Chapter 3 are then examined in order to determine which one best describes the Cl_2/He discharge. A preliminary experiment was used to obtain the general trends and significance of the input variables to the electrical signals of the plasma discharge. A complete experiment was then run with the relevant factors, and the impedance models were verified. In this chapter the test structures and the experimental designs are reviewed.

5.2 Initial Experiment

The initial experiment used in this study was designed for the purposes of another project. The objective of that project was to use advanced statistical techniques to develop a monitoring method suitable for real-time fault detection, fault diagnosis, and wafer state prediction [30]. Although not ideally suited to our modeling goals, part of these experi-

mental data could be used to verify the trends and relationships between the input parameters and the electrical signals of the Cl_2/He discharge.

5.2.1 Test Structure

The test structure was made from a 3-mask process. The final structure is shown in Figure 5.3. The exposed layers during the experiment included silicon dioxide, polysilicon, low temperature oxide (LTO), and photoresist. A complex structure of layers was chosen, to account for loading effects on the electrical measurements that a typical wafer may have in a real manufacturing environment. A detailed description of the process flow is included in Appendix B.

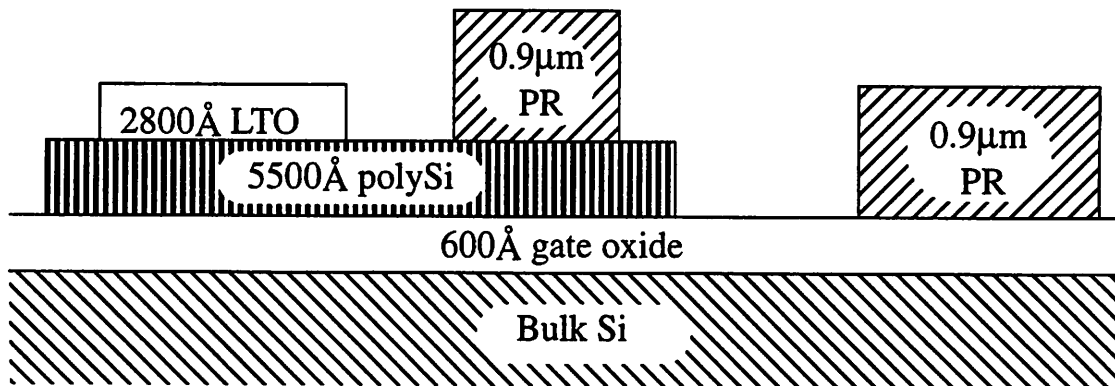


Figure 5.1 Test structure for the Initial Experiment.

5.2.2 Experimental Design

The etch process consisted of a pre-etch step for the removal of the native oxide and a main etch step for the etching of the different layers. The pre-etch step was constant for the entire experiment. A 2-level, fractional factorial (2^{5-1}) experiment was run around the centerpoint of the main etch step. The fractional factorial phase was not used in any our analysis. This phase of the initial experiment was designed for the project previously mentioned [30], and as such was not useful for our purposes. The centerpoint settings for both the pre-etch and main etch steps are listed in Table 5.1.

Table 5.1 Centerpoint Etch Recipes

Input Parameter	Pre-etch	Main Etch
Pressure (mtorr)	400	425
Power (Watts)	200	275
Gap (cm)	1.0	0.9
Cl ₂ (sccm) ^a	0	160
SF ₆ (sccm)	100	0
He (sccm)	0	380
He clamp (torr)	8.0	8.0

a. The flow rates are in units of sccm, "standard cubic centimeters per minute"

In addition to the fractional factorial experiment, "star" points were run (the Extended phase), and a subsequent experiment (the Diagnosis phase) was run approximately one month after the first two phases, see Figure 5.2.

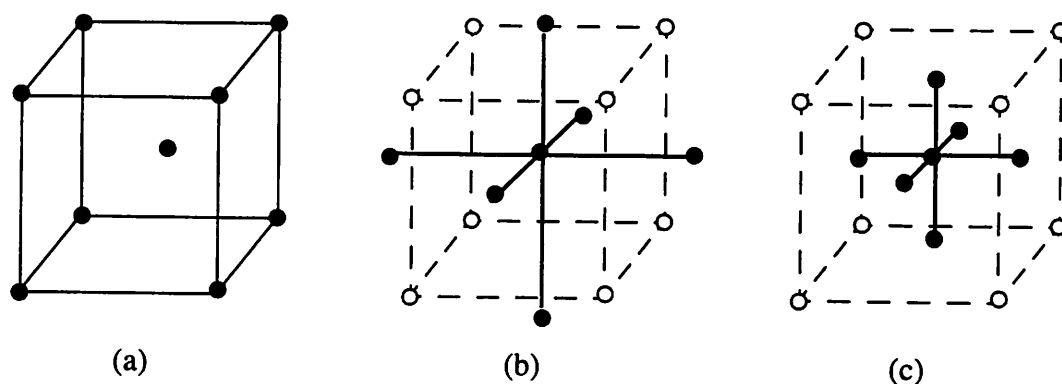


Figure 5.2 Depiction of three input settings for the (a) Fractional Factorial Phase (not used), (b) the Extended, and (c) the Diagnosis phase experiments.

In both the Extended and the Diagnosis phase, only one parameter was varied at a time. Because each parameter was varied one at a time, the significance of each input to the impedance model was verified, without fear of confounding effects from the other inputs. The parameters chosen were power (W), pressure (P), electrode gap (G), ratio of Cl₂:He (R), and the total gas flow of Cl₂ and He (T). At the time of the experiment it was felt that the ratio and total flows of the gases were more important to the output character-

istics of the wafer then the individual flows of Chlorine and Helium. The percent change for each input parameter, for each phase are summarized in Table 5.2. The next two sections discuss the Extended and the Diagnosis phase of the initial experiment.

Table 5.2 Change in Percent From Nominal

Parameter	Extended Experiment	Diagnosis Experiment
Pressure	$\pm 22.5\%$	$\pm 10\%$
Power	$\pm 22.5\%$	$\pm 10\%$
Gap	$\pm 17\%$	$\pm 10\%$
Flow Ratio	$\pm 22\%$	$\pm 10\%$
Total Flow	$\pm 22\%$	$\pm 10\%$

5.2.2.1 The Extended Phase

In this phase of the experiment each parameter was varied one at a time around the centerpoint settings. In between each experimental run, two dummy wafers were also run at the centerpoint settings. The percent change for each run is given in Table 5.2. Two centerpoints were also run in this phase. Table 5.3 list the randomized run order for this phase of the experiment. Included in Table 5.3 are the four centerpoint runs from the fractional factorial experiment.

Table 5.3 Randomized Extended Phase Runs^a

run #	P	R	W	G	T	lot #	wfr #
C1	425	0.42	275	0.9	540	8-1	5
C2	425	0.42	275	0.9	540	8-2	19
C3	425	0.42	275	0.9	540	8-2	16
C4	425	0.42	275	0.9	540	8-1	11
25	425	0.42	339	0.9	540	9-1	4
28	425	0.42	275	0.75	540	9-2	16
24	425	0.26	275	0.9	540	9-2	14
C5	425	0.42	275	0.9	540	9-1	1
29	425	0.42	275	0.9	660	9-1	6
22	329	0.42	275	0.9	540	9-2	17
27	425	0.42	275	1.5	540	9-1	2
26	425	0.42	213	0.9	540	9-2	18
C6	425	0.42	275	0.9	540	9-2	13
23	425	0.58	275	0.9	540	9-1	5
30	425	0.42	275	0.9	420	9-2	15
21	521	0.42	275	0.9	540	9-1	3

^a Bold face values indicate deviations from the centerpoint settings.

5.2.2.2 The Diagnosis Phase

One month after the initial two phases of the experiment were run, the Diagnosis phase was performed. The substantial time lag between the Extended and the Diagnosis phase was designed in order to capture the effects of time on the real time signals. This phase was similar to the Extended phase, with the only difference being the levels for each input parameter, as shown in Table 5.2. The randomized run order is summarized in Table 5.4.

Table 5.4 Randomized Diagnosis Phase Runs

run #	P	R	W	G	T	lot #	wfr #
V1	383	0.42	275	0.9	540	10	1
V2	425	0.42	275	0.9	540	10	14
V3	425	0.42	247	0.9	540	10	13
V4	425	0.42	275	0.85	540	10	8
V5	425	0.42	275	0.9	540	10	6
V6	425	0.38	275	0.9	540	10	18
V7	425	0.42	275	0.9	513	10	20
V8	425	0.42	275	0.9	540	10	4
V9	467	0.42	275	0.9	540	10	7
V10	425	0.42	303	0.9	540	10	17
V11	425	0.42	275	0.9	540	10	2
V12	425	0.42	275	0.95	540	10	16
V13	425	0.42	275	0.9	540	10	19
V14	425	0.46	275	0.9	540	10	15
V15	425	0.42	275	0.9	567	10	5

5.3 Verification Experiment

In this experiment the objective was to build models which would track the effects of RF power and pressure on the bulk and sheath impedances and also to verify the extent of the impedance models proposed. The variables for this experiment are power, pressure and Chlorine gas flow. The chlorine gas flow was also included because more data was needed to distinguish it from pressure, for the benefit of the project mentioned in the previous section [30]. What follows is a review of the test structure and the experiment designed.

5.3.1 Test Structure

Due to difficulties with some of the equipment in the Berkeley Microfabrication laboratory, the test structure for the verification experiment was simplified to a one mask process. This eliminated the use of the oxide etcher, which was out of statistical control at the time. The structure shown in Figure 5.3 was built following steps #1-5 of the process flow in Appendix B. This structure has different loading effects on the electrical signals of the Cl_2/He discharge, but the overall model should remain valid.

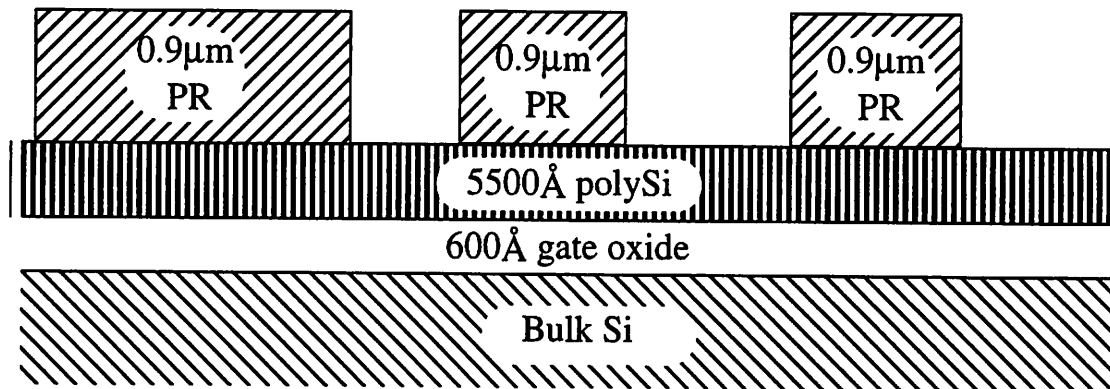


Figure 5.3 Test structure for the Verification Experiment.

5.3.2 Verification Experimental Design

This experiment was designed such that several points were run with only one input variable changing at a time. The relationships discussed in Chapter 4 could then be verified. This experiment focused on two parameters, RF power and pressure. In order to reduce the effects of experimental errors in the analysis, each point was replicated. Four centerpoints were also intermixed with the other runs. The Chlorine gas flow was also varied with all else constant. In addition to the aforementioned runs, RF power and pressure were varied concurrently to determine the extent to which the impedance models could predict multiple input variations. The levels at which the single faults were introduced were at $\pm 15\%$ and $\pm 7.5\%$ from nominal. Table 5.5 summarizes the input setting values for the verification experiment.

Table 5.5 Verification Experiment: Input settings

Input Setting	- 15%	- 7.5%	Center point	+ 7.5%	+ 15%
Pressure (mtorr)	361	393	425	457	489
Power (watts)	234	254	275	296	316
Cl ₂ (sccm)	136	148	160	172	184

Recall, in the initial experiment that total flow and the ratio of Chlorine and Helium were used as separate variables in the experiment, instead of the individual gas flows. In this experiment only Cl₂ was varied. A more realistic fault to model is when only one gas deviates from its centerpoint. The corresponding total flows and ratio for variations in Cl₂ are listed in Table 5.6.

Table 5.6 Ratio and Total Flows

Cl ₂ Gas Flow	136 sccm	148 sccm	160 sccm	172 sccm	184 sccm
Ratio ^a	0.356	0.389	0.421	0.453	0.484
Total Flow ^a	516	528	540	552	564

^a The above ratios and total flows were determined such that the gas flow for Helium remained constant (380 sccm).

For the runs in which both pressure and power were varied, the faults were injected at a level of $\pm 10.5\%$. The corresponding values are listed in Table 5.7.

Table 5.7 Pressure and Power settings for Interaction Terms

Input	+10.5%	-10.5%
Power	304W	246W
Pressure	470mtorr	380mtorr

The verification experiment was run in three separate blocks. This was done in the event the experiment was interrupted in the middle. Blocks one and two are the randomized runs, with one fault introduced at a time. Table 5.8 shows the chronological order for the faults at the $\pm 7.5\%$ level and Table 5.9 are the runs for the $\pm 15\%$ level. Block three is composed of the runs in which both RF power and pressure were varied (Table 5.10). For all three blocks, the experimental runs were replicated, and the centerpoints run four times. Therefore, a total of 36 runs were performed. Factors that could not be blocked, such as lot-to-lot differences, were randomized.

Table 5.8 Verification Experiment: Block I Randomized Runs

run#	P	W	Cl ₂	lot#	wfr#
11	425	275	148	15	8
6	425	296	160	15	23
10	425	275	172	14	19
8	425	254	160	15	3
5	425	296	160	14	18
1	457	275	160	15	9
4	393	275	160	14	20
7	425	254	160	14	24
13	425	275	160	14	15
2	457	275	160	15	14
9	425	275	172	15	20
12	425	275	148	15	19
3	393	275	160	14	13

Table 5.9 Verification Experiment: Block II Randomized Runs

run#	P	W	Cl ₂	lot#	wfr#
9	425	275	184	15	4
3	361	275	160	15	7
12	425	275	136	15	21
6	425	316	160	15	11
2	489	275	160	15	5
10	425	275	184	15	18
13	425	275	160	14	16
5	425	316	160	15	24
7	425	234	160	14	23
11	425	275	136	15	15
4	361	275	160	15	16
8	425	234	160	14	22
1	489	275	160	14	14

Table 5.10 Verification Experiment: Block III Randomized Runs

run#	P	W	Cl ₂	lot#	wfr#
10	425	275	160	15	17
7	470	304	160	14	17
1	380	246	160	15	6
6	380	304	160	15	2
3	470	246	160	15	13
9	425	275	160	15	10
4	470	246	160	15	1
2	380	246	160	15	22
8	470	304	160	15	12
5	380	304	160	14	21

5.4 Stray Impedance Characterization

An additional test was performed to characterize the stray impedances of the plasma etch system. The etcher was run at atmospheric pressure with no gases or wafer present in the chamber. Since the system was run with no gases and at low power settings, no plasma was struck. Under these conditions any measured impedance is attributed to the stray impedances in the chamber, in parallel with the capacitance due to the parallel plate electrodes. Though this may not be an exact measure of the stray impedance in the system, it gives us an idea of the magnitude of the stray capacitance and the resistive losses in the system. If the stray impedance is large enough, it may affect the accuracy of the proposed models and could be used to explain some of the discrepancies.

Recall from Chapter 3 that two alternative stray impedance networks were proposed to characterize the plasma etch system. In the first one all resistive losses are assumed negligible and only a stray capacitance is considered. The second network is of a more general form. A two-port network is used to represent the stray impedance network. Therefore, resistive and inductive losses are also accounted for. A two-port network is determined using a method proposed by Bauer and Penfield [20]. This technique “de-embeds” the actual impedance of the discharge by using an “unterminating” technique to determine the stray network. This is discussed in Section 5.4.2.

During these tests the gap was varied, to simulate different parallel plate capacitances, and thus load reactances. Measurements were taken at several power settings and averaged, for each gap separation. The resulting RPM-1 measurements are shown in Table 5.11.

Table 5.11 Stray Impedance Measurements

Gap	Z_{real}	Z_{imag}
2.006 cm	3.60	-34.64
1.508 cm	3.55	-33.81
1.008 cm	2.92	-31.90
0.906 cm	2.79	-31.41

5.4.1 Stray Capacitance Network

The corresponding parallel plate capacitance (C_{parallel}) is determined assuming a plate area of nine inches (22.77cm) and a plate separation given by the gap between the electrodes. If the resistive component is considered negligible in the stray impedance network, then the stray capacitance is:

$$C_{\text{stray}} = C_{\text{system}} - C_{\text{parallel}} \quad (\text{Farads}) \quad (5.1)$$

where C_{system} is the capacitance as measured from the RPM-1, and is defined as:

$$C_{\text{system}} = \frac{-1}{Z_{\text{imag}} \cdot \omega} \quad (\text{Farads}) \quad (5.2)$$

This assumes that the stray capacitance shunts the parallel plate capacitance, as shown in Figure 5.4. The resulting capacitances are summarized in Table 5.12.

Table 5.12 Parallel plate and Stray Capacitance

Gap (cm)	C_{parallel} (pF)	C_{system} (pF)	C_{stray} (pF)
2.0	18.03	338.9	320.9
1.5	24.04	347.4	323.4
1.0	36.05	368.1	332.0
0.9	40.06	373.8	333.7

The slight increase in the stray capacitance, observed as the gap separation is decreased, is due to the parallel plate component as the electrodes are brought closer together. Since the change corresponds to only a 3.84% variation in the stray capacitance, an average of the readings was taken. The resulting stray capacitance is 327.5pF.

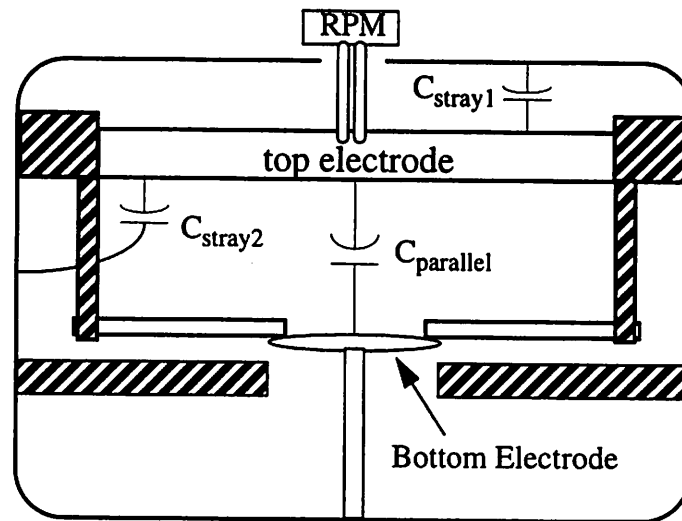


Figure 5.4 Plasma etch system with the stray capacitances annotated.

5.4.2 Two-Port Stray Network

A method introduced by Bauer and Penfield [20] is used to determine the impedance of a system under test, when the measurements are taken at a different location. Figure 5.5 illustrates this situation. The *embedded* network interferes with the true collection of the discharge impedance. This network would be composed of stray capacitances in the chamber, resistive losses, and line inductances.

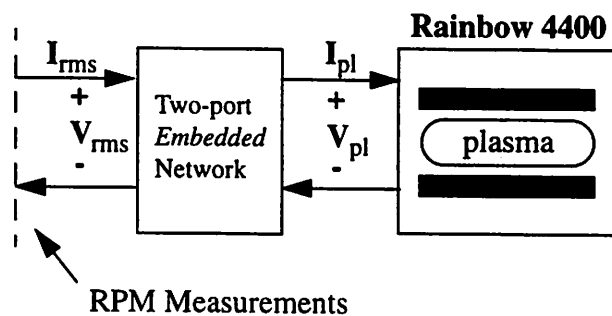


Figure 5.5 Stray embedded network as it relates to the plasma etch system in the Berkeley Microfabrication Laboratory.

In order to get at the “true” impedance of the discharge, the embedded network must be determined. One way to represent this network is by its two-port impedance parameters. The matrix representation of this is [31]:

$$\begin{bmatrix} V_{\text{rms}} \\ V_{\text{pl}} \end{bmatrix} = \begin{bmatrix} Z_{11} & Z_{12} \\ Z_{21} & Z_{22} \end{bmatrix} \cdot \begin{bmatrix} I_{\text{rms}} \\ -I_{\text{pl}} \end{bmatrix} \quad (5.3)$$

This leads to the input impedance as measured from the RPM-1:

$$Z_M = Z_{11} - \frac{Z_{12}Z_{21}}{Z_{22} + Z_{\text{pl}}} \quad (\Omega) \quad (5.4)$$

where Z_M is the measured impedance from the RPM-1, and Z_{pl} is the true load impedance of the system. Rewriting Eq (5.4) to consolidate terms, we get:

$$Z_M = \frac{|Z| + Z_{11}Z_{\text{pl}}}{Z_{22} + Z_{\text{pl}}} \quad (\Omega) \quad (5.5)$$

where $|Z| = Z_{11}Z_{22} - Z_{12}Z_{21}$ is the determinant of the z-matrix. Thus, with three independent measurements of known load impedances, the terms of the embedded stray network are determined. Unfortunately, due to measurement errors the resulting stray network may not be very accurate. For better results, additional runs are needed to minimize the error. The procedure to solve for the parameters is discussed in [20]. Using the data for the four different load reactances listed in Table 5.11, the z-matrix parameters were determined, and are summarized in the second column of Table 5.13. The results, however, are not physically realizable. The Z_{22} component has a negative real component, which is not possible.

Upon further investigation, it was determined that the experimental error was too large to accurately characterize the stray impedance of the plasma etch system at gap settings far from the centerpoint value (0.9cm). To realize the complete z-matrix, only three separate loads are needed. Depending on which three readings were used from Table 5.11, completely different stray impedance networks were obtained. Using the last three readings from Table 5.11, which are for gap settings closest to the centerpoint value of 0.9cm,

a physically realizable stray impedance network was obtained. The resulting parameters are summarized in column three of Table 5.13. Since such a large variance exist between the different measurements of the stray impedance, we should not expect to have an accurate characterization of the stray impedance. Further experiments are required, where the load impedance is better controlled. This will require the use of “dummy” loads in the plasma chamber. This, however, is not easily accomplished on an industrial etcher like ours. For the purposes of this study, the two-port stray network will be represented by the values listed in the third column of Table 5.13.

Table 5.13 Stray Impedance Parameters

Parameter	Z-matrix values ^a	Z-matrix values ^b
Z_{11}	3.341-36.768j	8.809-41.661j
Z_{22}	-85.177+85.094j	204.99-410.60j
$ Z $	4025.35+3086.28j	-9321.48-5820.967j
$Z_{12}=Z_{21}$	1.384-86.259j	36.96-85.70j

^a The z-matrix parameters were determined using all the data from Table 5.11.

^b The z-matrix parameters were determined using only the last three data points from Table 5.11.

5.5 Conclusions

Two experiments were designed and run. The objective of the first experiment, done in two phases, was to determine the trends and significance of each input variable to the electrical signals of the Cl_2/He discharge. The second experiment focused on two input parameters, RF power and pressure. The experiment was designed to determine which of the six impedance models proposed best characterize the Cl_2/He discharge, as the two inputs were varied. An experiment to determine the stray impedance of the discharge was also performed. Two different stray networks were calculated to try and characterize this aspect of the plasma etch system. The variance, however, was quite large for this last experiment and as a result the z-matrix is not believed to be very precise. The next chapter discusses the results obtained from these experiments.

Chapter 6

Results

6.1 Introduction

In this chapter we present the results from the experiments performed. In section 6.2 the first experiment, done in two phases establishes the trends and significance of each input variable with the electrical signals of the Cl_2/He discharge. Section 6.3 looks at the results from the second experiment, done for verification. Finally, the six impedance models proposed are analyzed in order to determine which best characterizes our plasma discharge.

Data from the Real Power Monitor (RPM-1) were collected at a rate of two samples/sec during the thirty second main etch step. The first ten samples of each experimental wafer were discarded in order to eliminate the brief period of instability that occurs when RF power is first turned on. An average of the remaining 50 samples is taken for each of the RPM-1 signals. Thus, one value for each RPM-1 signal is used to characterize each experimental wafer.

6.2 Initial experiment

In order to determine if the relationships proposed in Chapter 4 are accurate enough to characterize the Cl_2/He discharge, we plotted the real impedance versus the inverse of current density ($1/J_{\text{eb}}$). This was done for the data collected during the initial experiment described in section 5.2. For the full impedance model (Figure 3.3 iv) the real impedance is a combination of the bulk and sheath components:

$$Z_{\text{real}} = \frac{\Delta V_{\text{bulk}} \cdot \cos(\theta)}{A \cdot J_{\text{eb}}} + \frac{2R_{\text{sh}}}{1 + (\omega C_{\text{sh}} R_{\text{sh}})^2} \quad (\Omega) \quad (6.1)$$

where $R_{\text{bulk}} = (\Delta V_{\text{bulk}} \cdot \cos(\theta)) / (A \cdot J_{\text{eb}})$. The current density is varied by changing the RF power. The inverse of the current density was used because the real impedance of the bulk is a linear function of $1/J_{\text{eb}}$, if the product of the change in bulk potential and impedance phase is relatively constant, with varying RF power. Previous experimental work by Godyak, Piejak and Alexandrovich [10] have shown that the product of $\Delta V_{\text{bulk}} \cdot \cos(\theta)$ is constant for small discharge currents over a range of RF power settings.

The current density is determined by dividing the rms current measured by the area of the electrode. The resulting plot of Z_{real} versus $1/J_{\text{eb}}$ is shown in Figure 6.1. Two distinct sets of points are visible in the plot. The two sets of points correspond to the two groups of runs performed, in the Extended and the Diagnosis phase, respectively. Our data shows that a shift in the electrical signals occurred during the one month time lag. This may have transpired because of aging in the equipment, a dirty chamber, etc. This is unfortunate because the two sets of data can not be combined into one linear plot. However, some useful conclusions can be drawn.

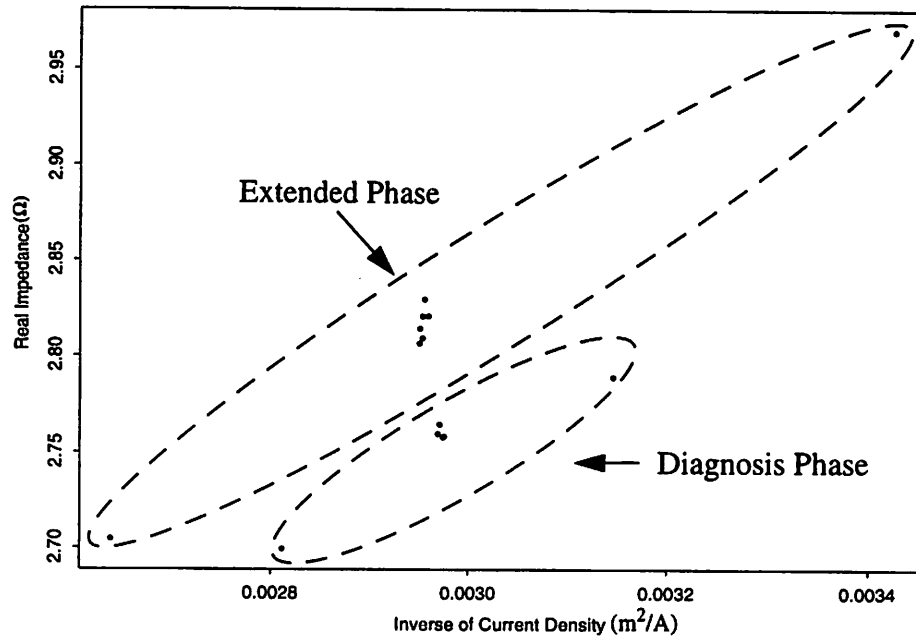


Figure 6.1 Real Impedance versus the Inverse of Current Density for the Extended and Diagnosis phase.

Even though in this instance models cannot be built because of insufficient data, the trends and the significance of each circuit component, with respect to the inputs, can still be verified. More importantly, the RPM-1 was able to detect a shift in the electrical state of the Cl_2/He discharge. This is important because it shows that the real time signals from the RF sensor reported a shift in the electrical state of the discharge, which would not have been otherwise detected. The major change in the signals was a shift in the y-intercept of the real impedance. This shift could be attributed to a change in the sheath parameters. One possible explanation is that the walls were getting coated from the etch process and this was causing a change in the amount of power dissipated. This would then be attributed to a change in the resistive component of the sheath, and could be an indication that it is time to vent the chamber and wipe it down. For the remainder of this section only the data from the Extended phase of the initial experiment is used to verify trends.

The data from the Extended phase in Figure 6.1, indicate a strong positive trend between the real impedance and $1/J_{\text{eb}}$. The results are in line with the linear relationship

expected between RF power and electron density, as discussed in Chapter 4. This is strong evidence that the bulk resistance has a major influence on the real impedance. However, not enough data points were collected to prove conclusively that the sheath resistance does not have an impact on the real impedance as RF power is varied. This is examined in the verification phase where more data points were taken. If the sheath resistance is an important component, then a nonlinear factor will be present in the plot of Z_{real} versus $1/J_{\text{eb}}$, as discussed in section 4.2.2.

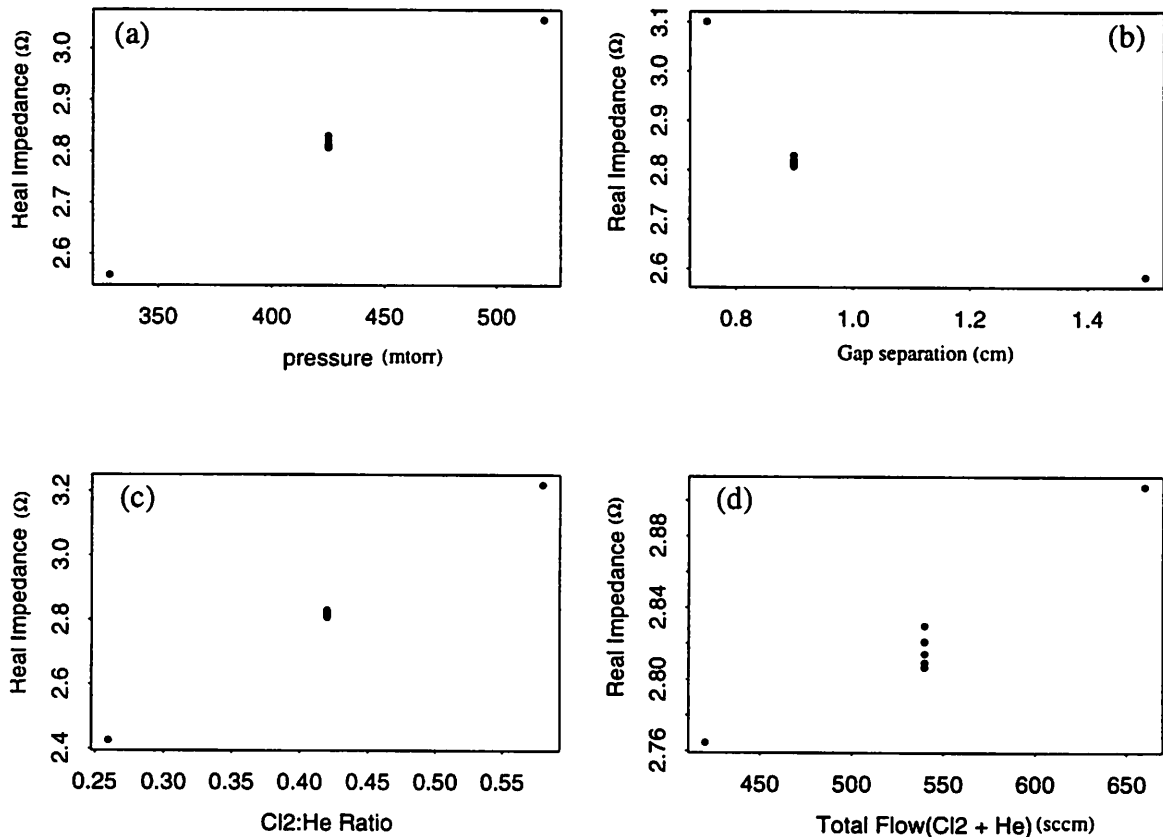


Figure 6.2 Real Impedance plotted versus the input parameters using Extended phase data: (a) Z_{real} vs. Pressure, (b) Z_{real} vs. Gap separation, (c) Z_{real} vs. Gas ratio, and (d) Z_{real} vs. Total Flow.

Figure 6.2 (a) through (d) show plots of the real impedance as a function of the other input parameters. As a function of pressure, the real impedance also displays a strong positive relationship. Lacking sufficient data, we can not determine whether or not this trend

is linear or quadratic. However, this data gives strong evidence that the product of pressure and electron mobility may in fact be constant, as indicated in Chapter 4 section 4.3.1.

For the gap separation a negative trend exist which looks quadratic. The upper setting for the gap setting was run at 1.5 cm, therefore, the runs are not centered around the centerpoint value of 0.90 cm. This was not intentional, but was instead an error on our part during the experiment. The upper gap setting should have been 1.05cm. Both the ratio and total flow of Chlorine and Helium have strong positive trends. However, the effect of the total flow on the real impedance is less dramatic.

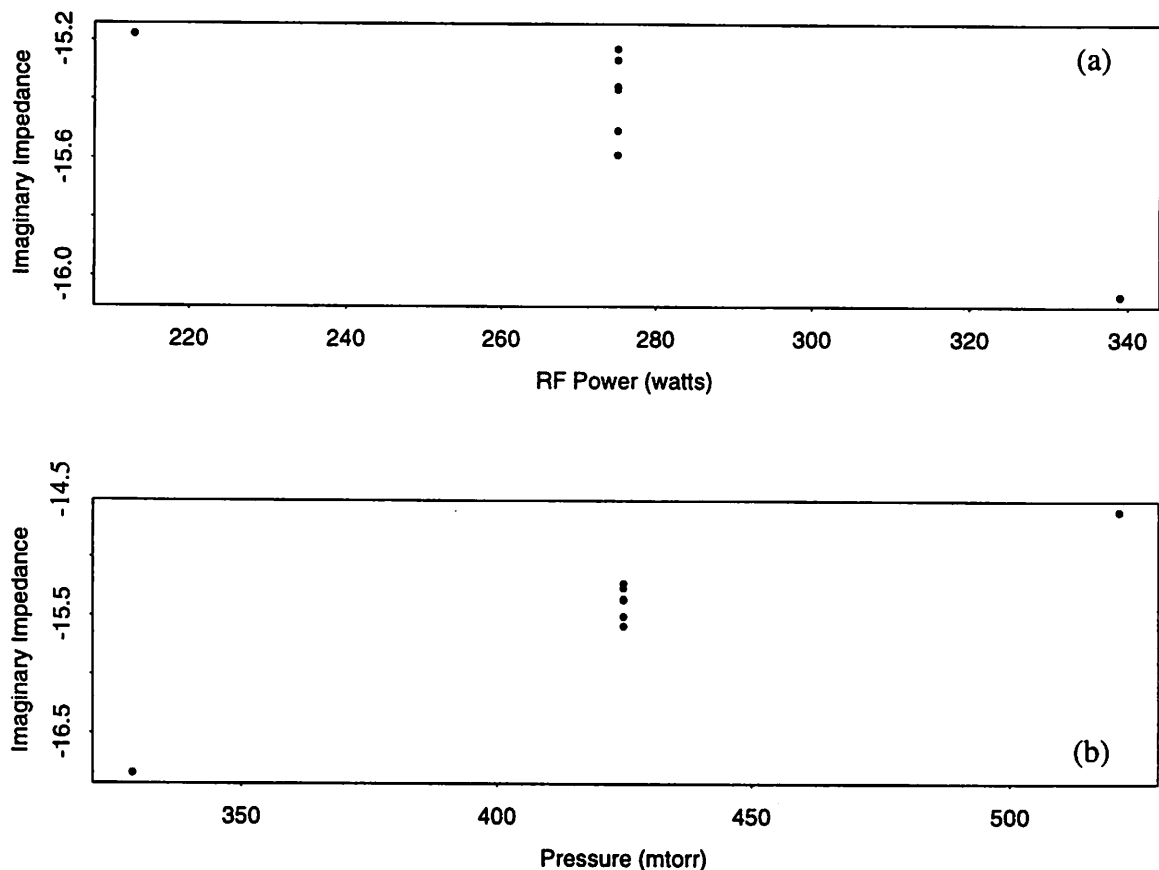


Figure 6.3 Imaginary Impedance versus (a) RF Power and (b) Pressure for the Extended phase.

Figure 6.3 shows the summary of how the imaginary impedance varies with power and pressure. Note that RF power has much less of an effect on the imaginary impedance than does pressure. The effect of pressure on the imaginary impedance is quite strong and

is attributed to the inverse relationship between pressure and the sheath thickness, as discussed in Chapter 4. Table 6.1 summarizes the trends for both the real and imaginary impedance as a function of the input parameters.

Table 6.1 Impedance trends with input variations

parameter	Real Impedance	Imaginary Impedance
RF Power	↘	↘
Pressure	↗	↗
Gap	↘	↘
Ratio	↗	↗
Total Flow	↗	↗

A simple statistical test was performed in order to determine which input parameters are more important to the electrical signals of the Cl_2/He discharge. If the variance for all the data points in the Extended phase, for each input parameter taken independently, is compared to the variance of the centerpoint readings, the effect of the input parameters on the impedance is quantified. The ratio of the two estimated variances follows the F-distribution [32]:

$$\hat{\sigma}_{\text{allpoints}}^2 / \hat{\sigma}_{\text{centerpoints}}^2 \sim F_{7,5} \quad (6.2)$$

The resulting F-values for each input parameter are summarized in Table 6.2. The 95% confidence interval for the F-distribution with 7 and 5 degrees of freedom is 4.88. At this level, RF power and total flow are not significant on the imaginary impedance. Also, the results for the gap separation are not entirely accurate because of the aforementioned error during the experimental run.

The resulting data should prove useful in tracking the behavior of the plasma discharge over a long period of time. The next section takes a closer look at the effects RF power and pressure have on the impedance models proposed in Chapter 3.

Table 6.2 F-distributions for the Input Parameters

parameter	Real Impedance ^a		Imaginary Impedance ^b	
	$\hat{\sigma}_{\text{allpoints}}^2$	F-value	$\hat{\sigma}_{\text{allpoints}}^2$	F-value
RF Power	0.00583	70.98	0.08243	4.32
Pressure	0.01784	244.40	0.39206	20.47
Gap	0.01928	264.01	3.181	166.06
Ratio	0.04506	671.18	0.9505	49.61
Total Flow	0.00158	21.69	0.0440	2.30

^a the variance of the centerpoints for the real impedance was 7.3014e-5

^b the variance of the centerpoints for the imaginary impedance was 0.019158

6.3 Verification Experiment

In this section the results from the verification experiment are discussed. The objective is to determine which one of the six impedance models proposed in Chapter 3 best describes the data collected for the Cl_2/He discharge. The results are presented in three subsections. The first subsection looks at the impedance models with no stray network included (Figure 6.4). The second subsection, includes a stray capacitance in the impedance model (Figure 6.13). Finally, subsection 6.3.3 will look at attempts to model the Cl_2/He discharge with a two-port stray network included in the plasma impedance model (Figure 6.18).

6.3.1 Impedance Models with no Stray Impedance Network

The first set of impedance models attempts to characterize the plasma discharge without regard to the stray impedances in our system. The two circuits are shown in Figure 6.4. The first circuit does not account for a resistive component in the sheath, while the second one does.

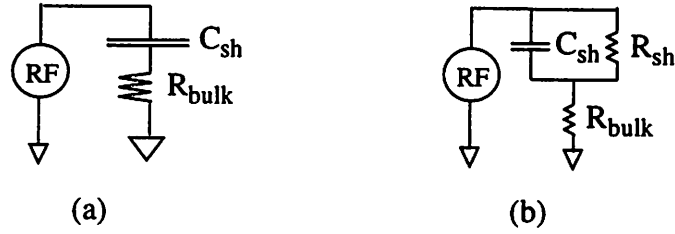


Figure 6.4 Impedance models of the Cl_2/He discharge. (a) with no sheath resistance, and (b) with the sheath resistance included.

6.3.1.1 Real Impedance

Before trying to model any of the effects described in Chapter 4, two assumptions must be verified. The first one is that the current density is a linear function with RF power and pressure. To this end least squares regression was used to fit a line to the data from the verification experiment. The result of this fit is shown in Figure 6.5. An R^2 value of 0.9982 was obtained when a line between current density and RF power was fitted. A correspondingly accurate fit was obtained between current density and pressure ($R^2 = 0.9854$).

The second assumption is whether or not the absorbed power is a linear function of the RF input power. Recall, that this assumption was used to make the connection between RF power and the bulk resistance, in section 4.2.1. The resulting fit of a straight line justifies the use of this assumption. The result is shown in Figure 6.6.

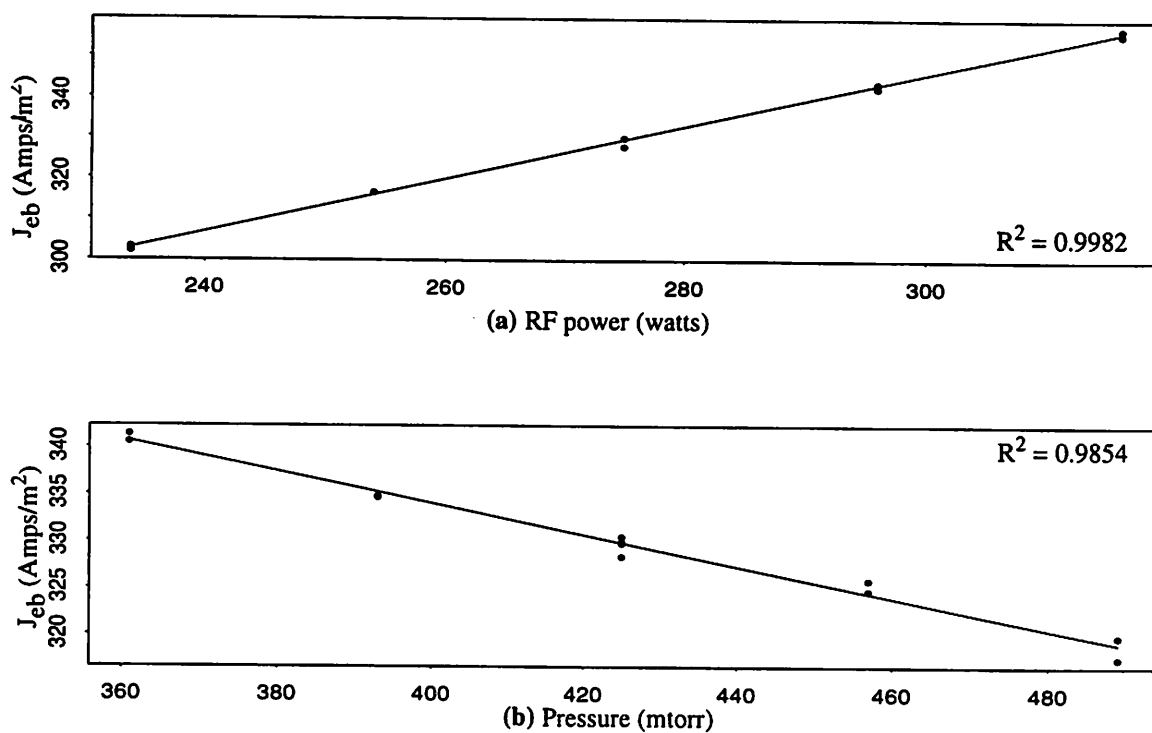


Figure 6.5 Current density as a function of (a) RF power and (b) pressure.

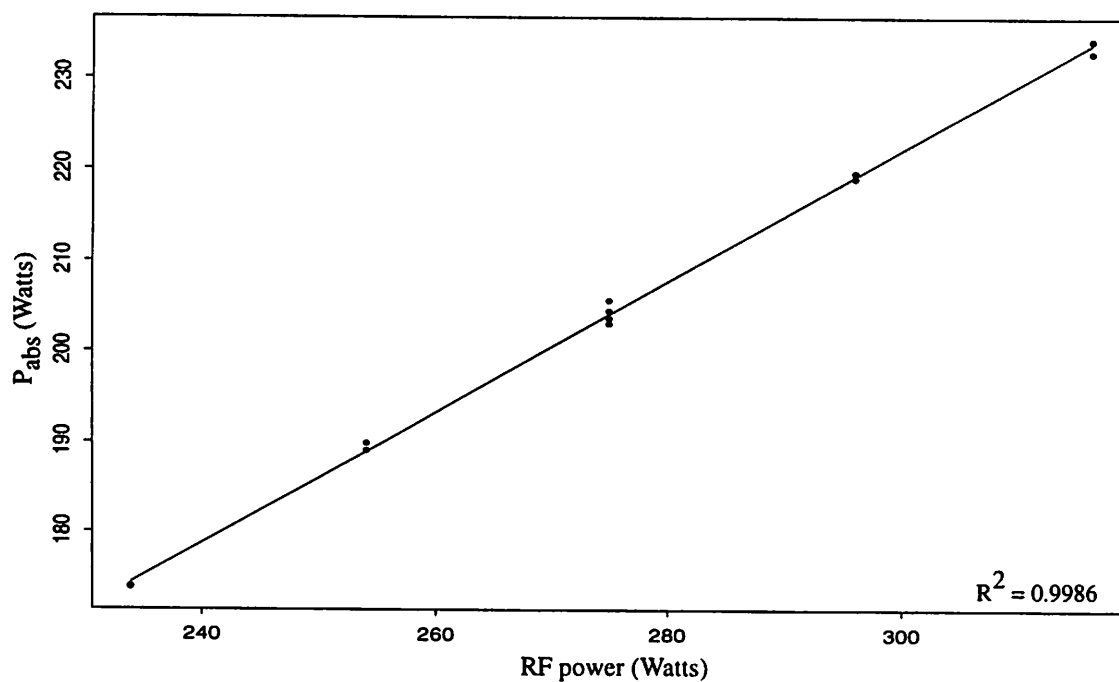


Figure 6.6 Absorbed power versus RF input power.

The first parameter examined was the real impedance as it varies with RF power. As mentioned in section 6.2 the real impedance as a function of $1/J_{eb}$ is linear if the bulk resistance dominates, and will deviate from this only if the sheath resistance is substantial. The characteristic equation is restated below for convenience:

$$Z_{\text{real}} = \frac{\Delta V_{\text{bulk}} \cdot \cos(\theta)}{A \cdot J_{eb}} + \frac{2R_{sh}}{1 + (\omega C_{sh} R_{sh})^2} \quad (\Omega) \quad (6.3)$$

The first term on the right hand side represents the bulk resistance. If this is the dominant term, it will vary linearly with RF power, as discussed in Chapter 4. Since we can control the current density through RF power, the plot of R_{sh} versus $1/J_{eb}$ should also be linear. The resulting least squares fit is shown in Figure 6.7. An R^2 value of 0.9098 was obtained for the linear fit. Even though the fit is strong, Figure 6.7 shows evidence of some underlying nonlinear function. A closer look at the sheath resistance may help to understand the root of this nonlinear effect.

If the second term in Eq 6.3 is expanded to include the equations defined for the sheath capacitance (eq.(3.8)) and resistance (eq.(3.10)), then the real part of the sheath impedance is:

$$\text{Re}(Z_{sh}) = \frac{2R_{sh}}{1 + (\omega C_{sh} R_{sh})^2} = \frac{\frac{1}{A\epsilon_0} \cdot \sqrt{\frac{m_i}{2qV_{sh}}}}{\frac{2}{9l_{sh}^2} + \frac{9m_i\omega^2}{16qV_{sh}}} \quad (\Omega) \quad (6.4)$$

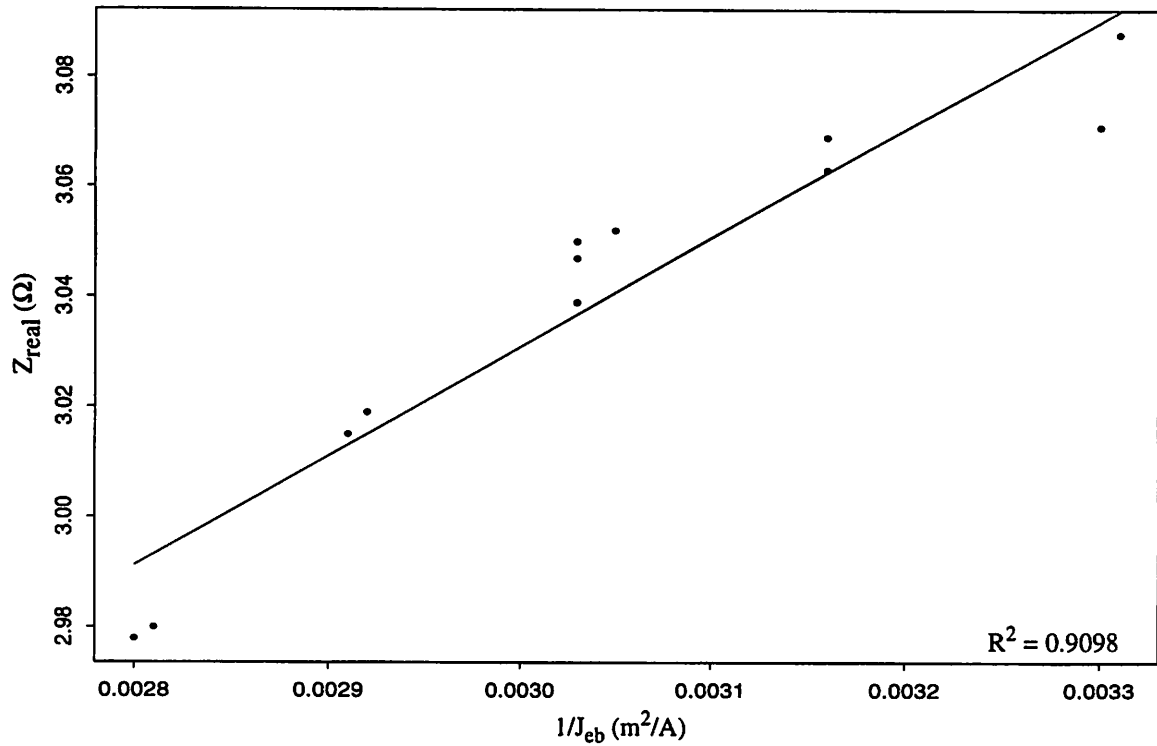


Figure 6.7 Z_{real} versus $1/J_{eb}$ for RF power varying only. The results are for a linear fit. Results for quadratic fit are shown in Figure 6.9.

If the sheath potential defined in Eq (6.4) is linear with RF power, then RF power will have a nonlinear effect on the real part of the sheath impedance. The sheath voltage is plotted versus RF power to confirm this linear relationship between the two parameters. Since V_{sh} is not directly measured, it is estimated. For a parallel plate system with equal-area electrodes, Ulacia and McVittie [8] define the plasma potential, with respect to the grounded electrode, to be:

$$V_{pl} = V_{rms} + \frac{V_{dc}}{2} \text{ (Volts)} \quad (6.5)$$

Both the rms voltage (V_{rms}) and the DC bias potential (V_{dc}) are reported by the Comdel RPM-1 sensor. The sheath potentials are then defined to be the plasma potential minus the potential at each respective electrode. With reference to the powered electrode, the sheath potential is:

$$V_{sh} = V_{pl} - V_{dc} = V_{rms} - \frac{V_{dc}}{2} \text{ (Volts)} \quad (6.6)$$

Equation (6.6) does not accurately represent our system, because of the asymmetric electrode areas in our plasma etcher. Most of the potential drop, in our case, will occur across the sheath corresponding to the smallest electrode area (the powered electrode). Eq (6.6) is defined for electrodes of equal dimensions. However, the sheath potential as represented here, can still be used to determine whether or not the sheath potential is linear with RF power. The fact that our system is asymmetrical should not be significant, because the sheath potential is being approximated by a linear combination of the rms voltage and the dc bias potential. If V_{rms} and V_{dc} are both linear with RF power, then any linear combination of these two parameters (i.e. the sheath potential) should also be linear with RF power. Figure 6.8 summarizes the results, when straight lines are fitted to the experimental data, with respect to RF power, for (a) the rms voltage, (b) the dc bias potential, and (c) the sheath potential as defined in Eq (6.6). The results confirm our assumption. The next step is to model the effect of the sheath resistance on the real impedance.

In order to separate the effects of the bulk and sheath resistance from the real impedance data, the linear component modeled line in Figure 6.7 was subtracted from the original real impedance data. The resulting data is thus the real part of the sheath impedance minus the linear part plus measurement error. Therefore, the form of the function to fit is defined by Eq 6.4. In this form, however, the function is nonlinear with the sheath potential. If the data is inverted, however, then linear regression can be used. The functional form of the fit is given, by inverting Eq 6.4:

$$\frac{1}{\text{Re}(Z_{sh})} = A\epsilon_o \sqrt{\frac{2q}{m_i}} \left(\frac{2}{9l_{sh}^2} \cdot \sqrt{V_{sh}} + \frac{9m_i\omega^2}{16\sqrt{V_{sh}}} \right) \quad (6.7)$$

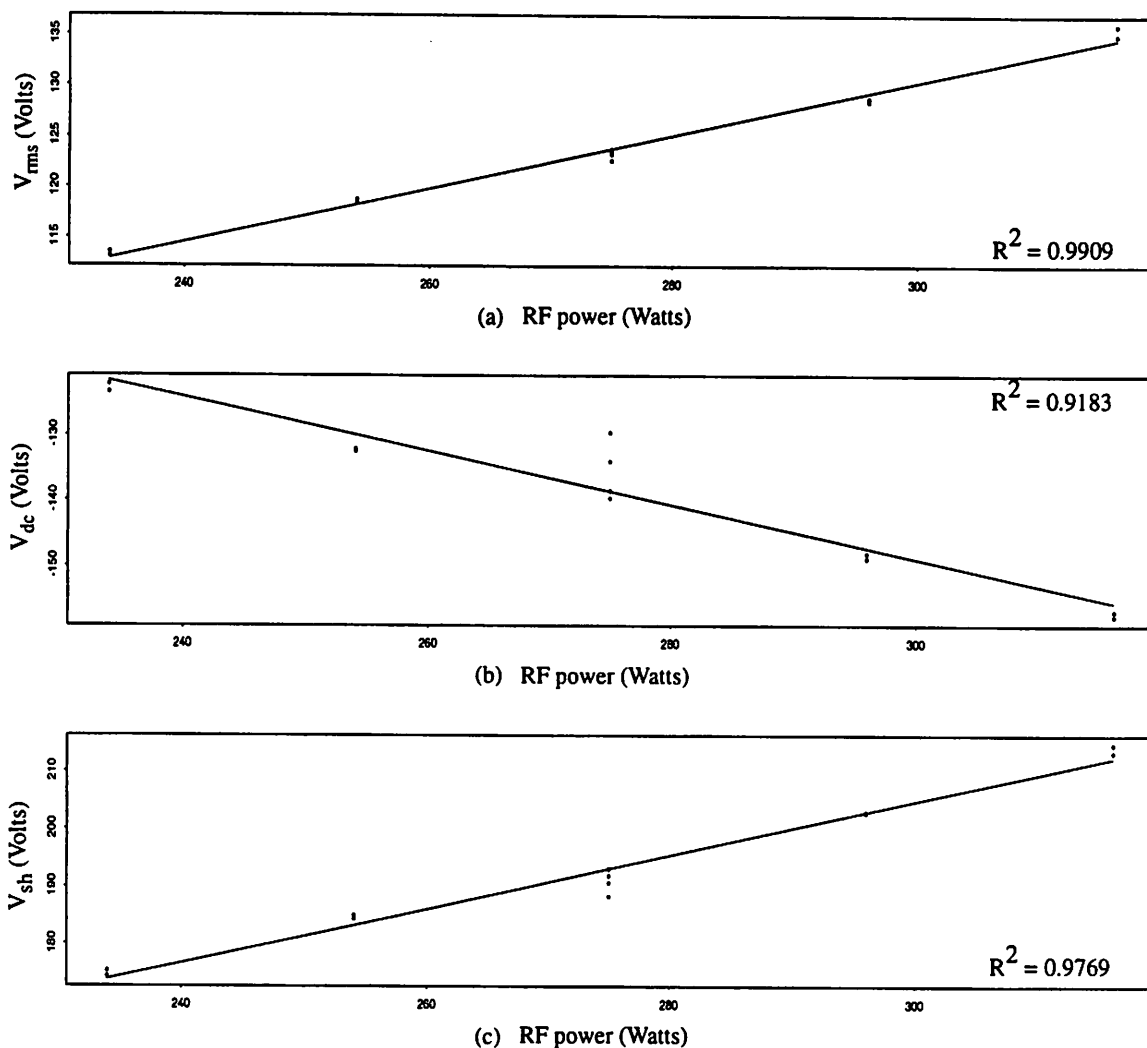


Figure 6.8 The (a) rms voltage, (b) dc bias potential and (c) sheath potential, as a function of the RF power.

After accounting for the sheath resistance a more accurate fit is obtained between the real impedance and RF power. The result of this analysis is shown in Figure 6.9. Though the sheath resistance is not a dominant component, it does slightly affect the real impedance. Therefore, a more accurate model is obtained if the sheath resistance is included in characterizing the Cl_2/He plasma discharge.

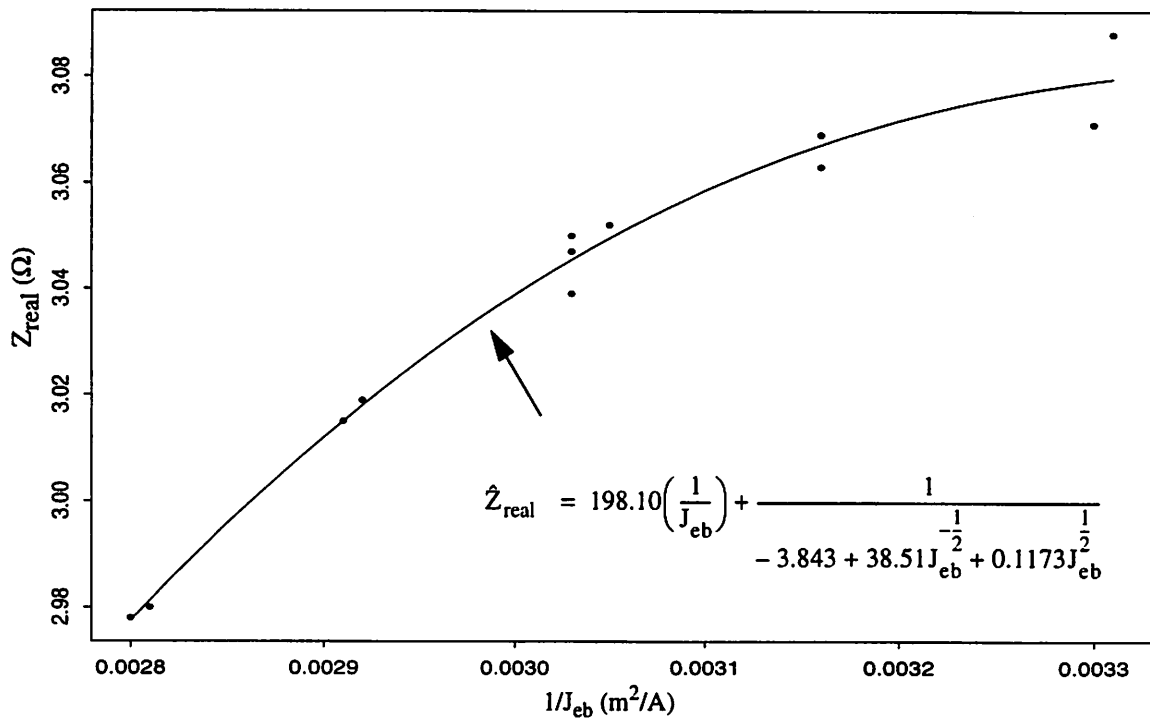


Figure 6.9 Z_{real} as a function of $1/J_{\text{eb}}$ taking into account the sheath resistance.

The real impedance is next modeled as a function of pressure. As stated in Chapter 4, the change in electron mobility with pressure causes a linear increase in the bulk resistance. The effect of pressure on the sheath impedance will depend on how dominant the first term in the denominator of Eq (6.4) is. Since pressure is inversely proportional to the sheath thickness, this term may contribute significantly to changes in the real impedance with pressure. Figure 6.10 shows the outcome of fitting a line to the data. The results show that a linear fit is significant ($R^2=0.9889$). The main effect is thus due to the relationship between the pressure and the bulk resistance.

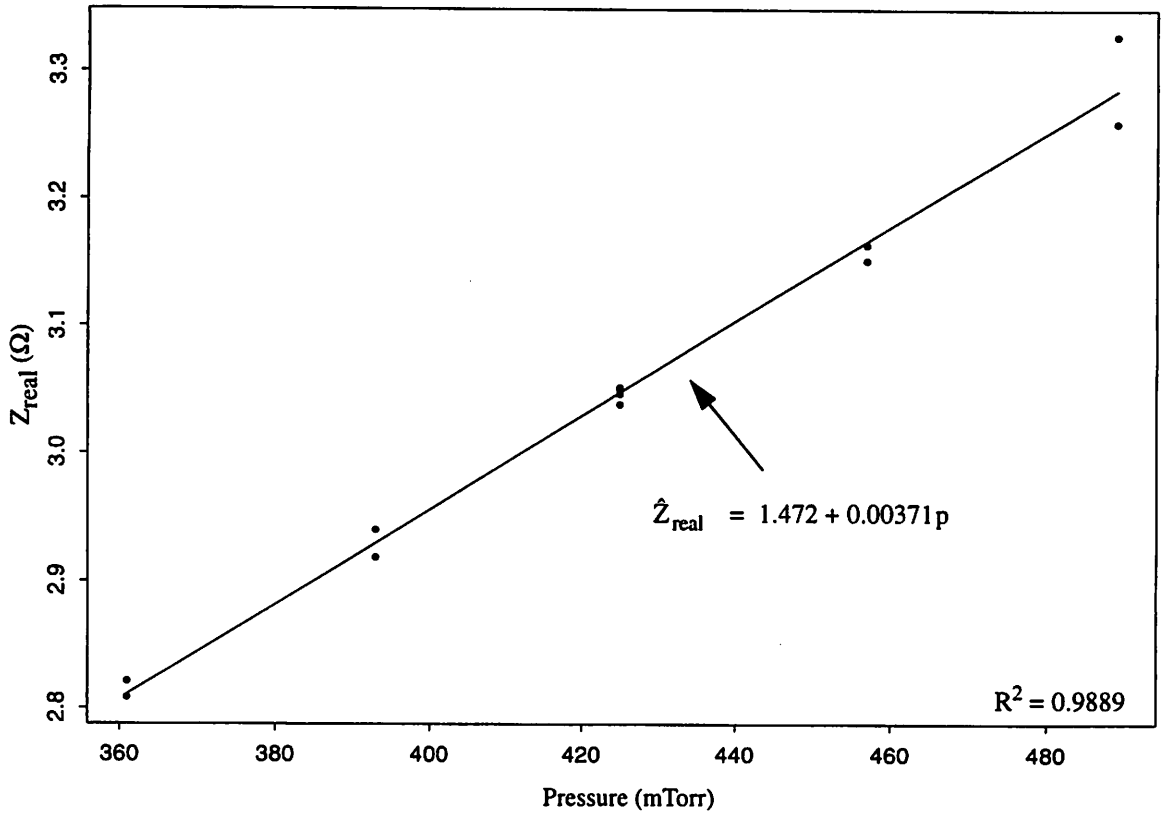


Figure 6.10 Real Impedance as a function of pressure.

6.3.1.2 Imaginary Impedance

The imaginary impedance is defined only by the components in the sheath. The imaginary impedance was defined in section 4.3.2 to be:

$$Z_{imag} = -\frac{1}{\frac{\epsilon_0 A}{l_{sh}} \left(\frac{2qV_{sh}}{\left(\frac{9}{4}\right)^2 l_{sh}^2 m_i \omega} + \omega \right)} \quad (\Omega) \quad (6.8)$$

In the initial experiment, RF power did not have a strong effect on the imaginary impedance. Plotting the imaginary impedance versus RF power (Figure 6.11) indicates that the RF power once again does not have a strong effect, except at the highest power setting.

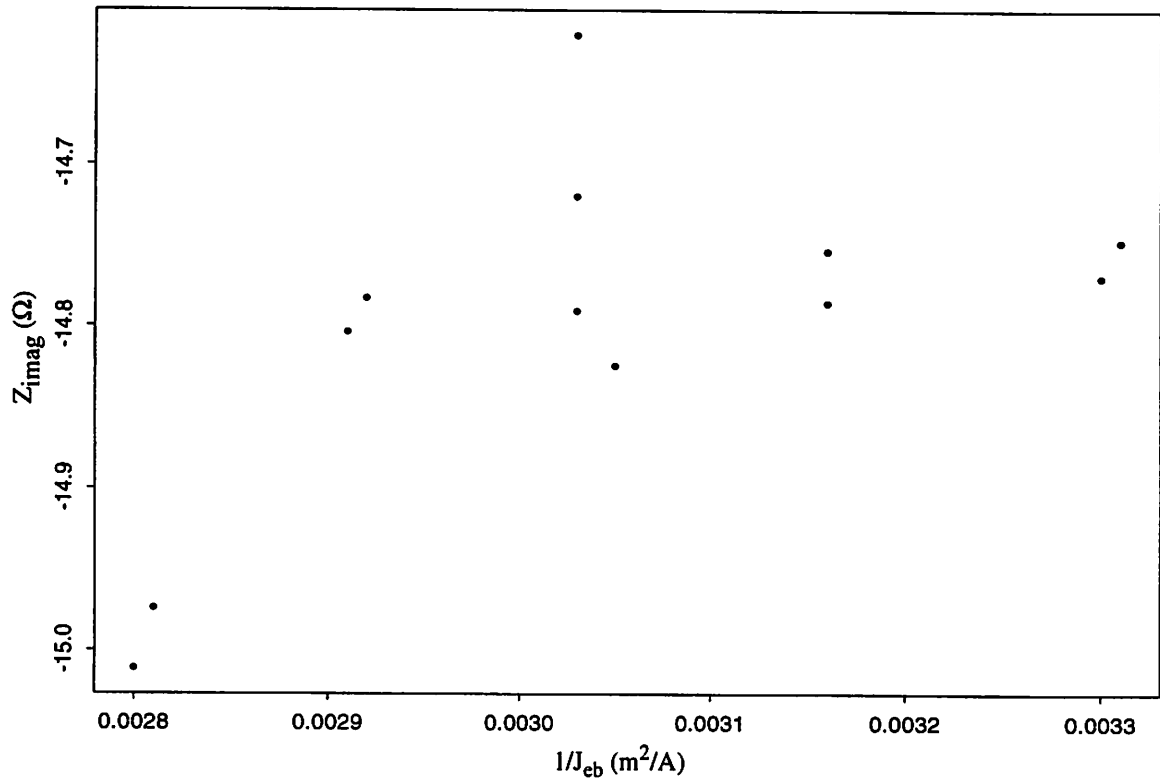


Figure 6.11 Imaginary Impedance as a function of $1/J_{eb}$ for RF power varying only.

One possible explanation for this phenomena is that at lower power densities the dominant term in Eq (6.8) is the second term in the denominator. The first term becomes dominant only in the upper power range. This makes sense since the sheath thickness is a weak function of RF power [11] and the sheath potential is linearly related to RF power as shown in Figure 6.8. If the first term in the denominator of Eq (6.8) were dominant this would cause the imaginary impedance to decrease linearly with RF power.

Another strong indicator that the imaginary impedance is relatively constant with RF power, comes from comparing the ratios of the variances and their corresponding F-statistic. The estimated variance of all the points, with RF power varying, is $\hat{\sigma}_{allpoints}^2 = 0.01092$, while the estimated variance for just the centerpoints is $\hat{\sigma}_{centerpoints}^2 = 0.00813$. This results in a ratio of 1.3438. The 95% confidence interval for an F distribution with 11 and 3 degrees of freedom is 8.77. Therefore, a safe approxi-

mation is to take the average of the imaginary impedance values for the power range under investigation and assume it is constant.

The imaginary impedance should increase linearly, as a function of pressure. This is a direct result of the strong inverse relationship between the sheath thickness and pressure as discussed in Chapter 4. The least squares fit of the data does indeed confirm this, as an R^2 value of 0.9894 was obtained. The results are shown in Figure 6.12.

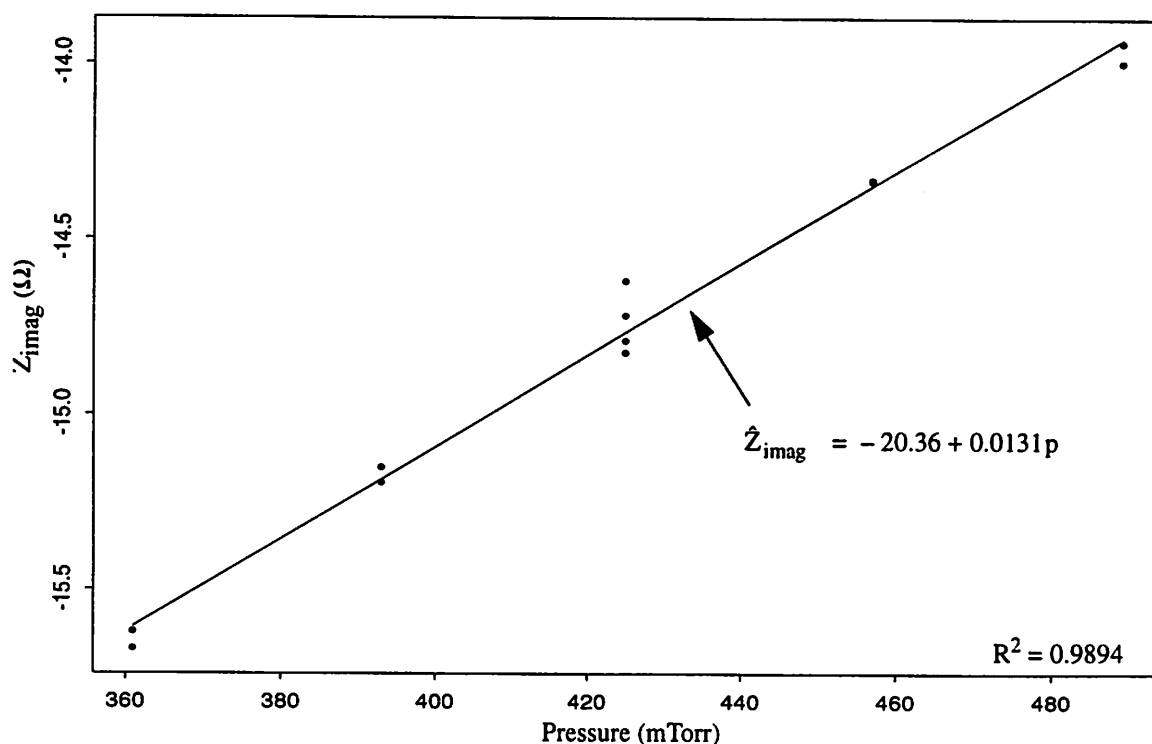


Figure 6.12 Imaginary impedance as a function of pressure.

6.3.1.3 Conclusions for Impedance Models with no Stray Impedance

The results confirm many of the relationships discussed in Chapter 4. The results seem to indicate that a series combination of the bulk resistance with a sheath capacitance explain many of the characteristics of the Cl_2/He plasma discharge. However, the inclusion of a sheath resistance eliminated some of the variability seen when modeling the real impedance, and thus a more accurate model was obtained. The next two subsections work with the same two impedance models, but also include a stray impedance network to explain some of the variability.

6.3.2 Impedance Models with Stray Capacitance

The next pair of impedance models includes a stray capacitance in the circuit model. The impedance models with a stray capacitance are shown in Figure 6.13. The experiment used to characterize the stray impedance was discussed in section 5.4. A value of 327.5 pF was determined for the stray capacitance (C_{st}) via low power, no plasma measurements. This translates into an impedance of $-35.84j \Omega$. The stray resistive losses was assumed negligible, relative to the stray capacitance.

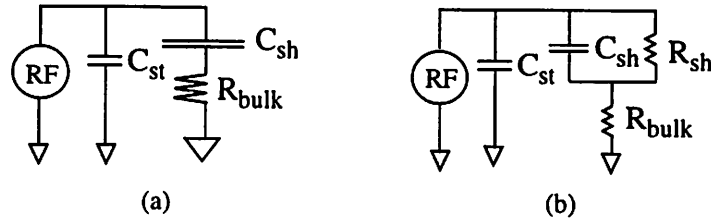


Figure 6.13 Impedance models with a stray capacitance factor included, (a) without the sheath resistance, (b) with the sheath resistance.

With the stray capacitance defined, the “true” impedance of the Cl_2/He plasma discharge was determined. Referring to Figure 6.14, the RPM-1 measures the total rms current (I_{rms}) and voltage (V_{rms}). To determine the “true” impedance of the plasma we use Kirchhoff’s current law around node 1 and solve for the plasma impedance (Z_{pl}). The result is:

$$Z_{\text{pl}} = \frac{V_{\text{rms}}}{I_{\text{rms}} - j\omega C_{\text{st}} V_{\text{rms}}} \quad (\Omega) \quad (6.9)$$

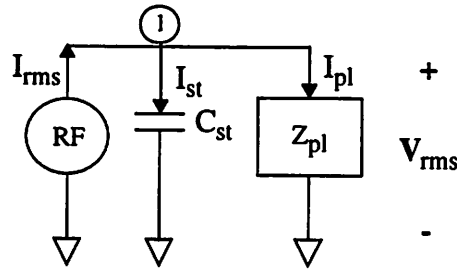


Figure 6.14 Schematic of system with stray capacitance and different currents annotated.

We begin again by looking at the plasma current density in order to determine if it is linear with RF power and pressure. The results are shown in Figure 6.15. The linear relationship between RF power and current density is quite strong, as evidenced by an R^2 value of 0.9908. However, the same is not true for the relationship between current density and pressure. The current density is weakly dependent on the pressure, after the correction for the stray impedance. The total variation is so slight (5.1 A/m^2), that the current density could be considered constant. The slight, statistically insignificant, positive trend which does exist is contrary to the expected relationship. We expect an inverse relationship between pressure and the current density, as discussed in Chapter 4.

The next two figures show the results for real and imaginary impedance as a function of RF power (Figure 6.16) and pressure (Figure 6.17). The results are not very promising. Only the imaginary impedance as a function of pressure is significant. There are two possible reasons why the results are not significant. (1) The assumption that the stray resistance was negligible may not be correct. This issue is addressed in section 6.3.3, when a general two-port model is used to characterize the stray impedance. (2) The second issue might relate to measurement sensitivity. The method used to determine the stray capacitance is somewhat crude. We assumed that the load in our system was a parallel plate capacitance, with the length and area determined by the electrode gap separation and top electrode area, respectively. The definition of the load is thus somewhat fuzzy. Fringe effects with the walls and the slight difference in electrode diameter will cause some dis-

crepancy in the results. To conclude that a stray capacitance is not necessary is premature. A better method to characterize the stray impedances is needed. This issue is further examined in the next section.

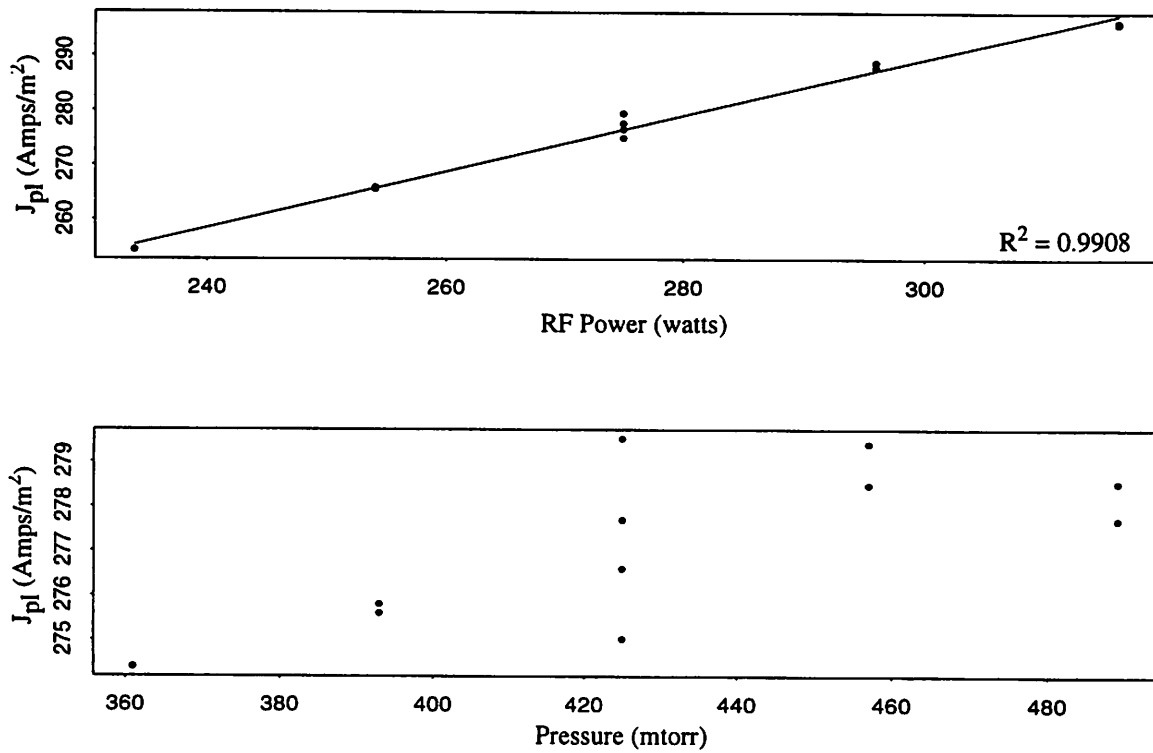


Figure 6.15 Current Density as a function of (a) RF power, and (b) pressure. Stray capacitance is included in the impedance model.

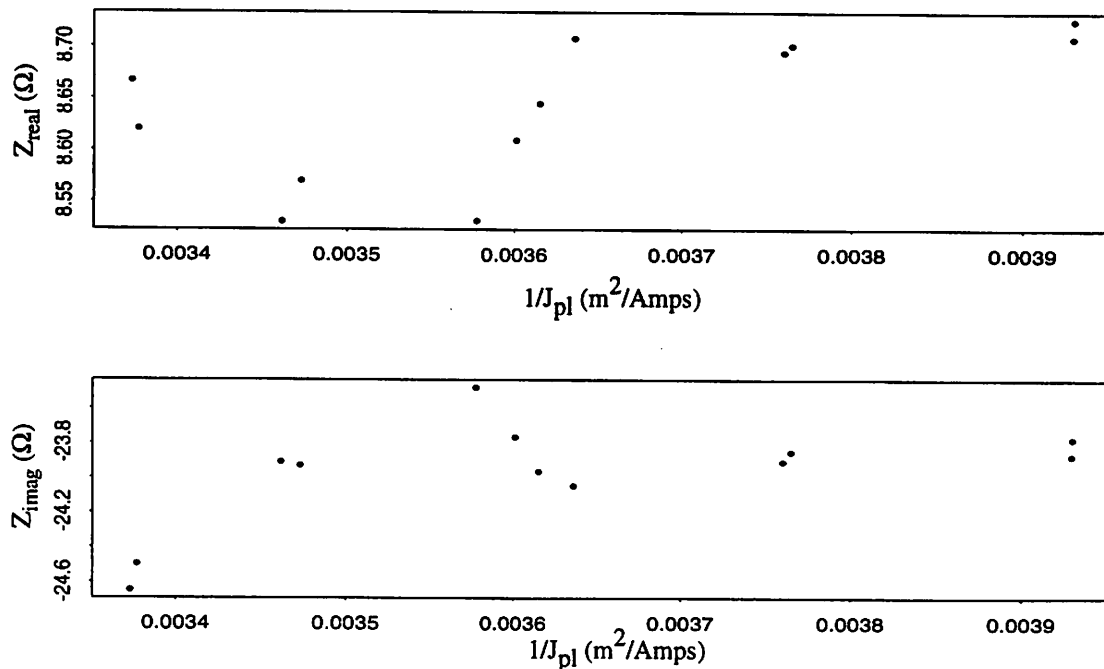


Figure 6.16 Results for the (a) real impedance and (b) imaginary impedance as a function of RF power. Stray capacitance is included in the impedance model.

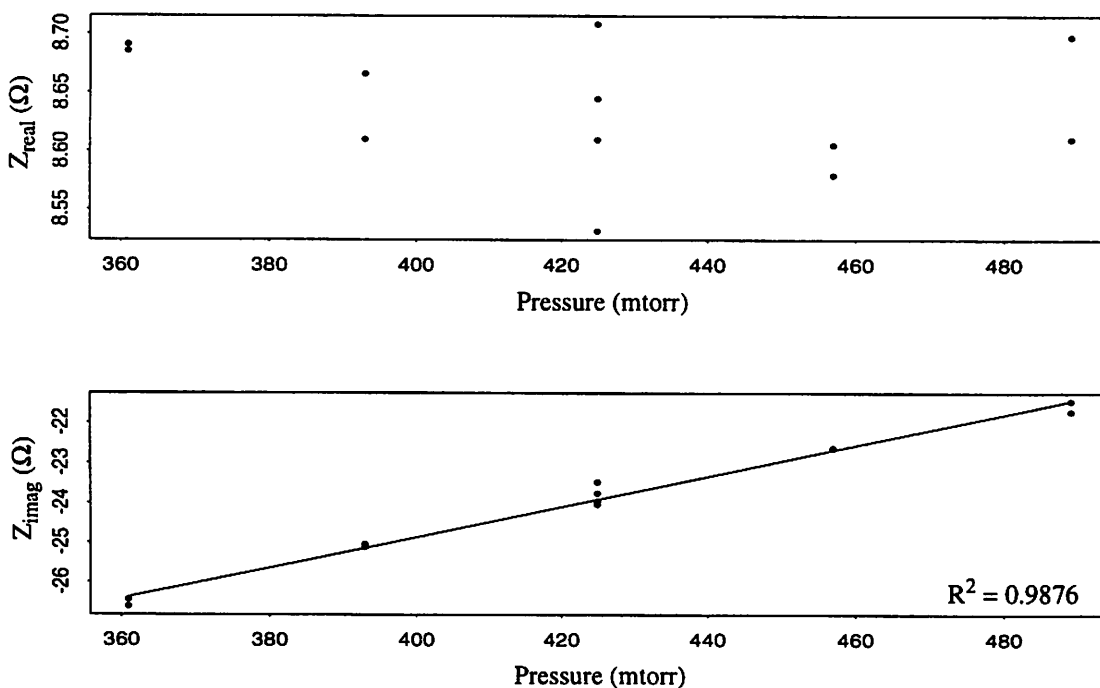


Figure 6.17 Results for the (a) real impedance and (b) imaginary impedance as a function of pressure. Stray capacitance is included in the impedance model.

6.3.3 Impedance Models with Two-Port Stray Networks

We now examine impedance models that include a two-port network to characterize the stray impedances of the Cl_2/He discharge. In this model, the stray resistances are not considered negligible relative to the stray capacitance. The impedance models used in this analysis are shown in Figure 6.18.

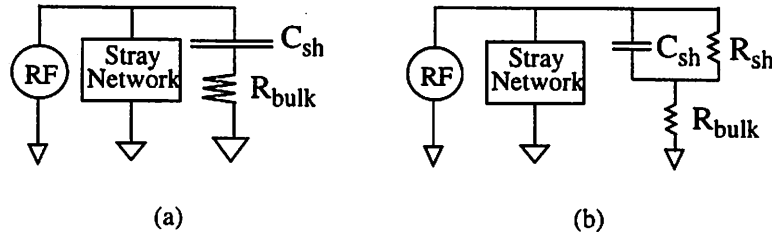


Figure 6.18 Impedance models with a two-port stray network included, (a) without the sheath resistance, (b) with the sheath resistance.

The two-port network was characterized using the experiment discussed in section 5.4.2. The results of the two-port network are summarized in Table 6.3.

Table 6.3 Two-port Parameters

Parameter	Value
Z_{11}	$8.809-41.661j$
Z_{22}	$204.99-410.60j$
$ Z $	$-9321.48-5820.967j$
$Z_{12}=Z_{21}$	$36.96-85.70j$

Referring to Figure 6.19, for a known two-port network and measured RF voltage and current, the plasma current and voltage can be calculated. The relationships are:

$$I_{pl} = \frac{-V_{rms} + Z_{11}I_{rms}}{Z_{12}} \quad (\text{Amps}) \quad (6.10)$$

$$V_{pl} = Z_{21}I_{rms} - Z_{22}I_{pl} \quad (\text{Volts}) \quad (6.11)$$

The plasma impedance is then simply calculated as:

$$Z_{pl} = V_{pl}/I_{pl} \text{ } (\Omega) \quad (6.12)$$

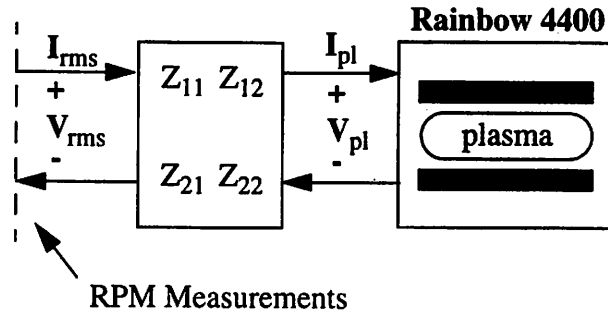


Figure 6.19 Two-port Network with RF and Plasma signals denoted.

Once again, we begin by verifying the assumption that current density is constant with RF power and pressure. The results for this analysis are shown in Figure 6.20. An R^2 value of 0.9942 was obtained for the fit between current density and RF power. The fit between current density and pressure was not significant. An R^2 value of 0.4227 was calculated.

Analyzing the data for the real and imaginary impedance as a function of RF power (see Figure 6.21) the resulting relationships are not very promising. As a function of RF power the plasma impedance comes out inductive and the real impedance is negative. This would mean that the plasma discharge is creating power, which is not physically possible. The results seem to indicate that the experiment used to characterize the stray impedance in our system is not accurate enough. The experimental error, coupled with the assumptions made regarding our parallel plate load impedance are not precise enough to accurately characterize the stray impedances in our system.

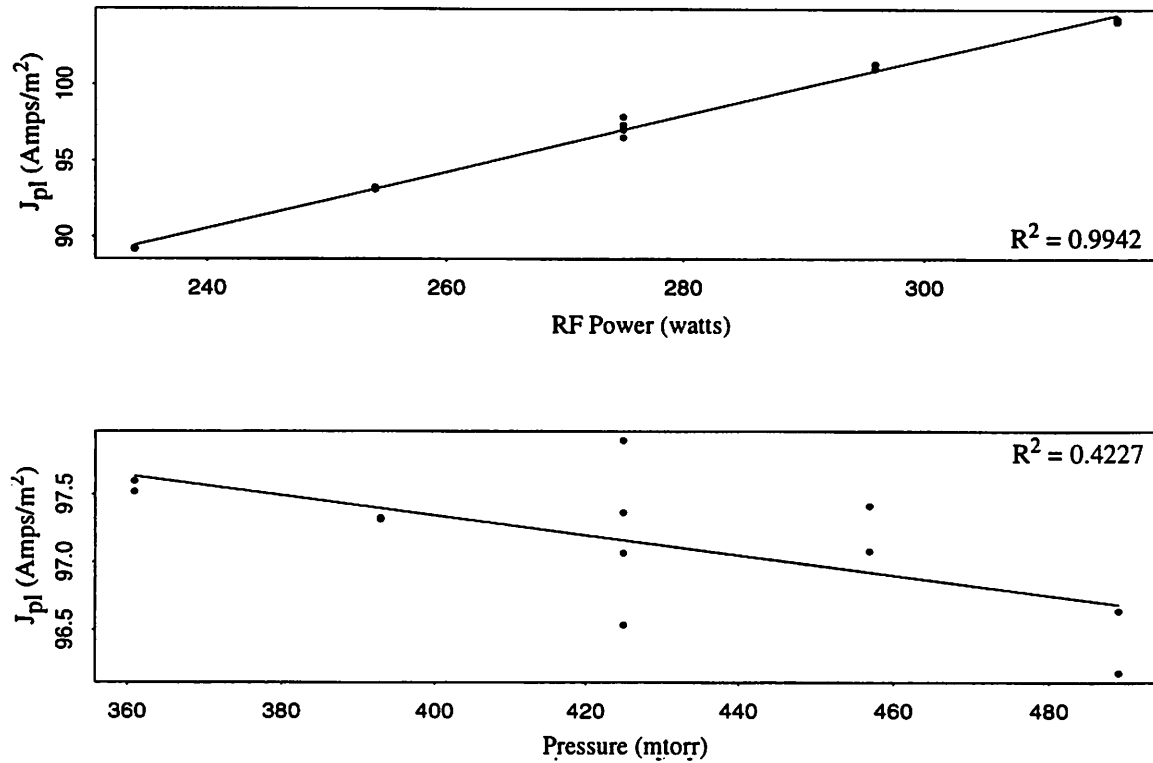


Figure 6.20 Current density as a function of (a) RF power and (b) pressure. Two-port stray network included in the impedance model.

As a function of the pressure, the real and imaginary impedance have a strong linear relationship. A least squares fit of the data confirms this, as shown in Figure 6.22. R^2 values of 0.9093 and 0.9889 were obtained for the real and imaginary impedance versus pressure, respectively. However, the extracted plasma impedance, as a function of pressure, is not physically obtainable as mentioned before.

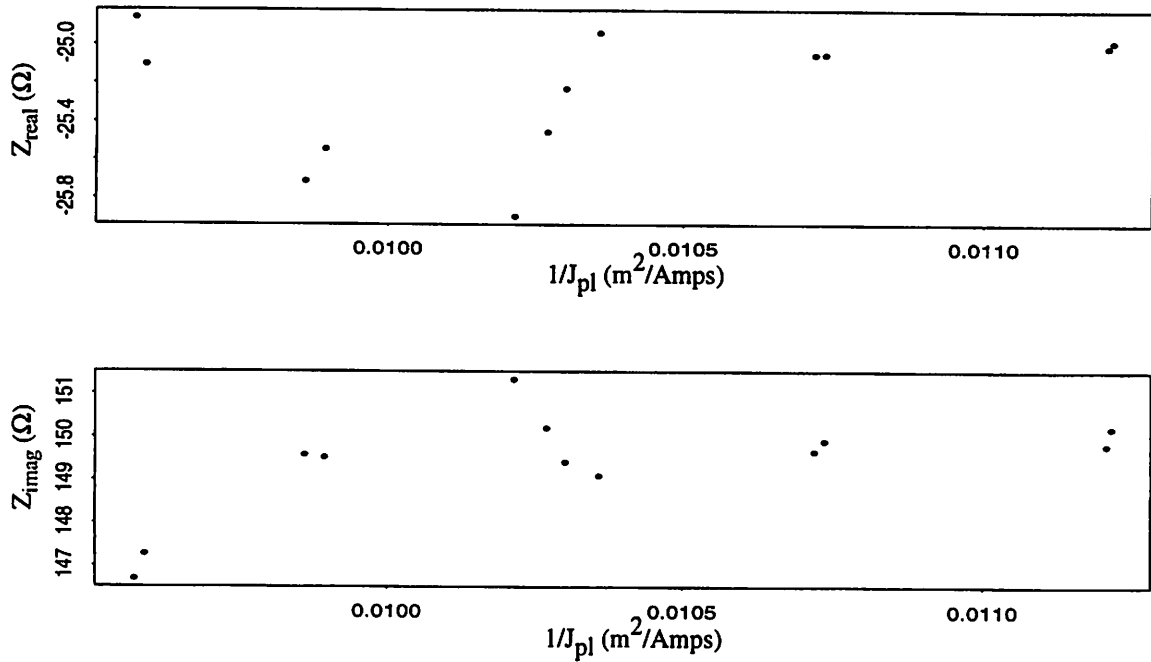


Figure 6.21 Real and Imaginary impedance as a function of RF power ($1/J_{\text{eb}}$). Two-port stray network included.

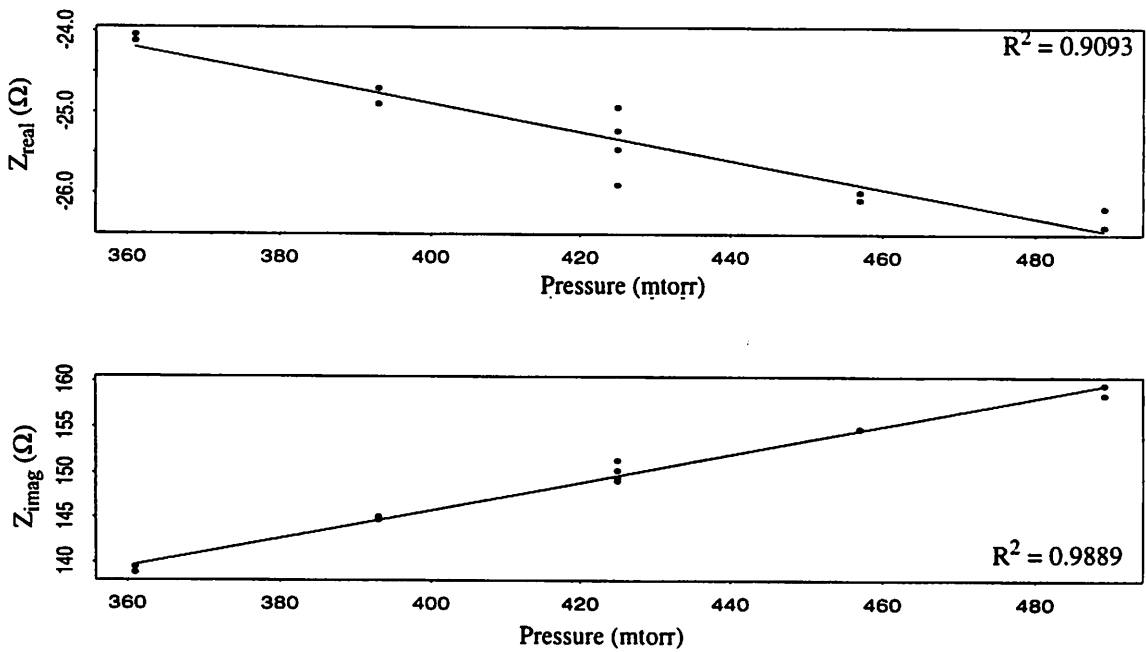


Figure 6.22 Real and Imaginary impedance as a function of pressure. Two-port stray network included.

The results obtained by including the two-port stray network are not an accurate representation of a Cl_2/He plasma discharge. The main reason for this stems from the experiment used to characterize the stray impedance network. The experimental error was too great to ignore and proper characterization of the stray impedance in our system was thus impossible. A more controlled experiment is required, where the load impedance is more precisely set.

For the impedance models proposed, the Cl_2/He discharge was best modeled with a bulk resistance in series with a parallel combination of a sheath capacitance and resistance. This impedance model is depicted in Figure 6.23 and detailed in section 6.3.1. The next section takes a look at how one may be able to track the Cl_2/He impedance discharge when both RF power and pressure simultaneously shift from their centerpoint values.

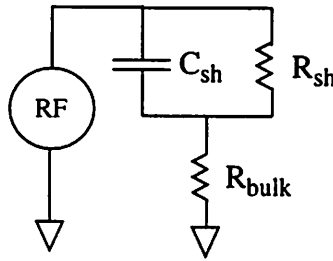


Figure 6.23 Impedance Representation of a Cl_2/He discharge.

6.3.4 Power-Pressure Interactions

In this section we look at how well the impedance model shown in Figure 6.23 tracks the electrical behavior of the Cl_2/He discharge, when both RF power and pressure are varied. Recall, in the verification experiment that the third block consisted of runs in which both RF power and pressure were varied. Using the extracted parameters determined in section 6.3.1 the expected real and imaginary impedance can be determined for the input settings used in the third block of the verification experiment. The models for the extracted parameters were built using the data from the first two blocks of the experiment. Therefore, the data from this phase can be used to determine how well the extracted models characterize the Cl_2/He discharge when multiple inputs are varied.

6.3.4.1 Real Impedance

In order to separate the effects of RF power and pressure from the discharge impedance, a closer look at the extracted parameters is required. The real impedance as a function of RF power and pressure are shown in Eqs (6.13) and (6.14). Note that Eq 6.13 was extracted for the current density when RF power was only varied.

$$\hat{Z}_{\text{real}} \left(\frac{1}{J_{\text{eb}}} \right) = 198.10 \left(\frac{1}{J_{\text{eb}}} \right) + \frac{1}{-3.843 + 38.51 J_{\text{eb}}^{-\frac{1}{2}} + 0.1173 J_{\text{eb}}^{\frac{1}{2}}} \quad (\Omega) \quad (6.13)$$

$$\hat{Z}_{\text{real}} (p) = 1.472 + 0.00371p \quad (\Omega) \quad (6.14)$$

The relationship between pressure and the real impedance was attributed to a linear increase in the bulk resistance. Since the pressure does not substantially effect the real part of the sheath impedance, only the first term is affected in Eq 6.13. The pressure will effect the linear component (or the slope) of the relationship between Z_{real} and RF power, as shown in Figure 6.24. Thus, for a given pressure, the new slope (or the characteristic line in Figure 6.24) can be determined. We can then use Eq 6.13 to determine the real impedance of the discharge, as RF power is varied.

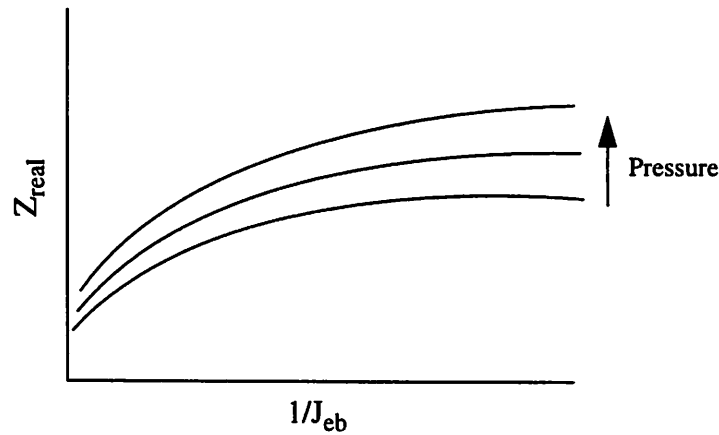


Figure 6.24 Z_{real} versus $1/J_{\text{eb}}$ power and pressure

6.3.4.2 Imaginary Impedance

Since the imaginary impedance is weakly dependent on RF power variations, as shown in Figure 6.11, we will assume that it is constant and approximate it with the average of the data points (-14.799Ω). Therefore, the only shift in the imaginary impedance is due to the pressure. This relationship was determined to be linear and the extracted line was:

$$\hat{Z}_{\text{imag}} = -20.36 + 0.0131p \quad (\Omega) \quad (6.15)$$

6.3.4.3 Results

Tables 6.4 and 6.5 show the results of the calculated versus experimental values for the real and imaginary impedance, respectively, as RF power and pressure were varied from their centerpoint values. The average of the two experimental runs for each setting were reported under the measured column. The match between the measured and the calculated data is quite promising. The slight inaccuracy can be attributed to the assumption that the imaginary impedance remains constant over the RF power range.

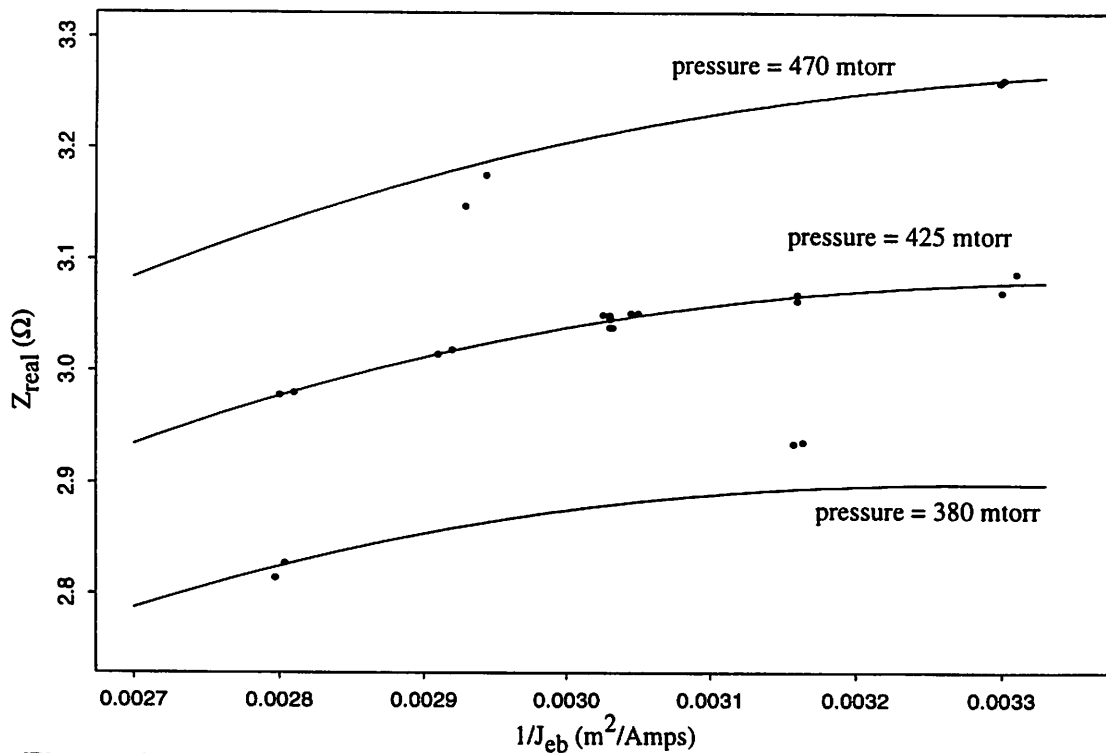
Table 6.4 Results for the Real Impedance with Multiple Effects

RF Power (Watts)	Pressure (mtorr)	Z_{real} (meas) (Ω)	Z_{real} (calc) (Ω)	Percent Difference
247	381	2.936	2.897	1.33%
247	469	3.261	3.259	0.06%
275	425	3.047	3.047	0%
303	381	2.821	2.823	0.07%
303	469	3.162	3.174	0.38%

Table 6.5 Results for the Imaginary Impedance with Multiple Effects

RF Power (Watts)	Pressure (mtorr)	Z_{imag} (meas) (Ω)	Z_{imag} (calc) (Ω)	Percent Difference
247	381	-15.210	-15.368	1.04%
247	469	-14.190	-14.214	0.17%
275	425	-14.739	-14.791	0.35%
303	381	-15.639	-15.368	1.73%
303	469	-14.292	-14.214	0.55%

If the extracted lines are plotted for both power and pressure variations, a plot similar to that of Figure 6.24 is obtained. The results are shown in Figure 6.25. As the pressure is increased, a slight increase is seen in the linear component of the real impedance as a function of the inverse current density.

**Figure 6.25** Real impedance versus the inverse of current density for different pressure and RF power variations.

6.3.5 Conclusions from the Verification Experiment

Accurate fits were obtained between the experimental data and the impedance models that included a sheath resistance. The impedance model shown in Figure 6.23 accurately characterizes the electrical behavior of a Cl_2/He plasma discharge. Table 6.6 is a summary of the different parameters extracted from the impedance models, without any stray impedance characterization.

Table 6.6 Summary of Extracted Relationships

Impedance Model	Expression	R^2	Form
Impedance Models without any Stray Impedance Network	$J_{eb}(P_{RF})$	0.9982	linear
	$J_{eb}(p)$	0.9854	linear
	$P_{abs}(P_{RF})$	0.9986	linear
	$V_{rms}(P_{RF})$	0.9909	linear
	$V_{dc}(P_{RF})$	0.9183	linear
	$V_{sh}(P_{RF})$	0.9769	linear
	$Z_{real}(P_{RF})$	0.9098	linear
	$Z_{real}(P_{RF})^a$	0.9098 / 0.8084	quadratic
	$Z_{real}(p)$	0.9889	linear
	$Z_{imag}(P_{RF})$	---	constant
	$Z_{imag}(p)$	0.9894	linear

^a The two R^2 values reported are for the linear and nonlinear components of the real impedance extracted, respectively.

Chapter 7

Conclusions

An impedance model has been developed to characterize a Cl_2/He plasma discharge for variation in RF power and pressure. The results from an experiment performed in the Berkeley Microfabrication Laboratory verify that the impedance model of the form shown in Figure 6.23 tracks the electrical behavior of the Cl_2/He discharge quite well. Physical understanding was used to arrive at the relationships between RF power and pressure, and the impedance model. Using these relationships, the real and imaginary impedance were extracted from the experimental data with great accuracy.

Before arriving at this circuit, several impedance models were investigated, which accounted for different factors. The basic impedance model was composed of elements which describe the current transport mechanisms in the bulk and sheath region. From this analysis, two impedance models were proposed, one with and one without the sheath resistance. The experimental results show that for the operating conditions used, the sheath resistance does indeed influence the electrical behavior of the Cl_2/He discharge.

The stray impedances in the discharge were also analyzed. Two models were proposed to account for this. The first network was composed of just a stray capacitance. The second stray impedance network was represented with a two-port model. The results indicate that the experiment and method used to characterize the stray impedance is not accurate enough to describe our system. A better controlled experiment is required.

The impedance model was also tested when both RF power and pressure were varied simultaneously. The extracted model was used to determine the impedance of the plasma discharge, at new RF power and pressure settings. A comparison with experimental data was performed and the results are quite promising.

With an impedance model in place diagnosis on the plasma etcher may be performed. When drifts in the electrical signals are detected, analysis on the real and imaginary impedance can help in determining the cause of the problem, and thus eliminate any lengthy downtime. By detecting the shift in the electrical behavior of the plasma discharge early on, we also hope to reduce the effect a large drift may have on the output characteristics of the wafer.

Further study remains in developing physical relationships between the impedance models and the output characteristics of the wafer. These characteristics include the etch rate, uniformity, selectivity and anisotropy. The existing relationships should prove useful in this analysis.

References

- [1] V. M. Donnelly, "Optical Diagnostic Techniques for Low Pressure Plasmas and Plasma Processing", *Plasma Diagnostics. Volume 1: Discharge Parameters and Chemistry*, edited by O. Auciello and D. L. Flamm, 1989.
- [2] J. W. Coburn and M. Chen, "Optical Emission Spectroscopy of Reactive Plasmas: a Method for Correlating Emission Intensities to Reactive Particle Density", *J. Appl. Phys.*, Vol. 51, 1980, pp. 3134.
- [3] I. Langmuir and H.M. Mott-Smith, *Gen. Elec. Rev.*, Vol 26, 1923, pp. 731.
- [4] B.E. Cherrington, "The use of Electrostatic Probes for Plasma Diagnostics - a Review", *Plasma Chem. Plasma Proc.*, Vol. 2, 1982, pp. 113.
- [5] B. Lipschultz, I Hutchinson, B. LaBombard, and A. Wan, "Electric Probes in Plasmas", *J. Vac. Sci. Technol. A*, Vol 4, 1986, pp.1810.
- [6] H. R. Koenig, L. I. Maissel, "Application of RF Discharges to Sputtering", *IBM J. Res. Develop.*, March 1970, pp. 168-171.
- [7] J. H. Keller and W. B. Pennebaker, "Electrical Properties of RF Sputtering Systems", *IBM J. Res. Develop.*, Vol. 23(no. 1), 1979, pp. 3-15.
- [8] J. I. Ulacia and J. P. McVittie, "In-Situ Monitoring of Electrical Parameters for Dry Etching", *Mat. Res. Soc. Symp. Proc.*, Vol. 98, 1987, pp. 203-209.
- [9] K. D. Allen, H. H. Sawin, M. T. Mocella, and M. W. Jenkins, "The Plasma Etching of Polysilicon with CF_3Cl /Argon Discharges", *Journal of the Electrochemical Society*, Vol 133(no. 11), 1986, pp. 2315-2325.
- [10] V. A. Godyak, R. B. Piejak, and B. M. Alexandrovich, "Electrical Characteristics of Parallel-Plate RF Discharges in Argon", *IEEE Transactions on Plasma Science*, Vol. 19(no. 4), August 1991, pp. 660-676.
- [11] E. S. Aydil and D. J. Economou, "Theoretical and Experimental Investigations of Chlorine RF Glow Discharges", *Journal of the Electrochemical Society*, Vol. 139(no. 5), May 1992, pp. 1396-1412.
- [12] B. Andries, G. Ravel, and L. Peccoud, "Electrical Characterization of Radio-Frequency Parallel-Plate Capacitively Coupled Discharges", *J. Vac. Sci. Technol. A*, Vol. 7(no. 4), Jul/Aug 1989, pp. 2774-2783.

- [13] A. J. van Roosmalen, "Plasma Parameter Estimation from RF Impedance Measurements in a Dry Etching System", *Appl. Phys. Lett.*, Vol. 42(no. 5), March 1983, pp. 416-417.
- [14] J. W. Butterbaugh, L. D. Baston, and H. H. Sawin, "Measurement and Analysis of Radio Frequency Glow Discharge Electrical Impedance and Network Power Loss", *J. Vac. Sci. Technol. A*, Vol. 8(no. 2), Mar/Apr 1990, pp. 916-923.
- [15] B. E. Thompson, K. D. Allen, A. D. Richards, and H. H. Sawin, "Ion Bombardment energy distributions in Radio-Frequency Glow-Discharge Systems", *J. Appl. Phys.*, Vol. 69(no. 6), March 1986, pp.1890-1903.
- [16] B. E. Thompson and H. H. Sawin, "Polysilicon Etching in SF₆ RF Discharges", *Journal of the Electrochemical Society*, Vol. 133(no. 9), September 1986, pp.1887-1895.
- [17] A. J. van Roosmalen, W. G. M. van den Hoek, and H. Kalter, "Electrical Properties of Planar RF Discharges for Dry Etching", *J. Appl. Phys.*, Vol. 58(no. 2), July 1985, pp. 653-658.
- [18] D. B. Ilic, "Impedance Measurement as a Diagnostic for Plasma Reactors", *Rev. Sci. Instrum.*, Vol. 52(no. 10), October 1981, pp. 1542-1545.
- [19] P. Rummel, "Monitoring and Control of RF Electrical Parameters Near Plasma Load", *Industrial Heating*, May 1991.
- [20] R. F. Bauer and P. Penfield, "De-embedding and Unterminating", *IEEE Transactions on Microwave Theory and Techniques*, Vol. 22(no.3), March 1974, pp. 282-288.
- [21] Lam Research, "Rainbow Plasma Etch Systems," *Operations and Maintenance Manuals*, vol. 1, revision 3.0, March 1992.
- [22] *Lamstation Rainbow*, version 3.6, Brookside Software, 1991.
- [23] Chromex Spectrograph, Albuquerque, New Mexico
- [24] Real Power Monitor (RPM-1), Comdel Inc.
- [25] D. M. Manos and D. L. Flamm, *Plasma Etching an Introduction*, Academic Press, New York, 1989.
- [26] A. J. van Roosmalen, J. A. G. Baggerman, and S. J. H. Brader, *Dry Etching For VLSI*, Plenum Press, New York, 1991.

- [27] G. L. Rogoff, J. M. Kramer, "A model for the Bulk Plasma in an RF Chlorine Discharge", *IEEE Transactions on Plasma Science*, Vol. 14(no. 2), April 1986, pp. 103-111.
- [28] M. Meyyappan and T. R. Govindan, "Modeling of Electronegative Radio Frequency Discharges", *IEEE Transactions on Plasma Science*, Vol. 19(no. 2), April 1991, pp. 122-129.
- [29] R. C. Jaeger, *Introduction to Microelectronic Fabrication, Volume V*, Addison-Wesley Co., New York, 1990.
- [30] S. F. Lee, *Semiconductor Equipment Analysis and Wafer State Prediction System Using Real-Time Data*, Ph.D. Dissertation, University of California Berkeley Memorandum No. UCB/ERL M94/104, Dec. 1994.
- [31] K. L. Su, *Fundamentals of Circuits, Electronics, and Signal Analysis*, Waveland Press Inc., Prospect Heights, Illinois, 1978.
- [32] G. E. P. Box, W. G. Hunter, and J. S. Hunter, *Statistics for Experimenters*, John Wiley & Sons, New York, 1978.

Appendix A

Modifications to the Real Power Monitor Software

This appendix reviews the modifications made to the RPM-1 software which accompanied the unit. The following changes were made in order to make the data collection easier during the etch process:

1. Automate the data collection, at our request.
2. Collect data only when there is power is applied.
3. Each wafer logged in separate files.
4. Transmit the data files to a local area network of workstations automatically.

All changes were made to the “Data Logger”^a option in the RPM-1 software. This option is reached from the main menu of the software. The software is written in c language and the filename is called “rpm4.c”. The integer number in the filename is used to denote which version of the code is being used. The most recent version will have the highest number (i.e. rpm4.c is more recent than rpm3.c). What follows is a brief discussion of the software changes made.

Automatic Data Collection

In the *rpmlog* routine a flag was created (*auto_coll*) which is set when automatic data collection is desired. The user is prompted to choose between automatic and manual data collection when he/she first enters the “Data Logger” function of the software. When this variable is set, a loop is created which continuously looks at the output signals from the

RPM-1 sensor. A message is printed to the screen to let the user know that the system is in automatic mode and is waiting for real data from the RPM-1 sensor (“Standby mode”).

Another variable was established in the event the plasma etcher stalls. This variable (smtime) is the total time allocated for each wafer in the system. The user is also prompted for this value once in the “Data Logger” function. This value will change depending on the specific etch process. A typical value previously used was 200 seconds.

Collection of real RPM-1 data

During a typical etch process, there are many periods of idle time. These are purposely placed in the etch recipe to stabilize the gas flows and chamber pressure, for instance. The RPM-1 data, during these periods, are not useful and should not be collected. To eliminate this data from our files the `rp` variable was monitored. This variable tracks the real power absorbed by the plasma etch system. Only data with a real power value greater than 50 watts is stored to a file. This value was chosen somewhat arbitrarily. The only criteria used to set this value was that it be low enough not to eliminate any data when an RF power is on, and the value be high enough to eliminate any noisy signals when the system is off. Since our etch process called for an RF power setting of 275 watts during normal operation, the value was chosen to assure the collection of this data. Therefore, data is collected only when RF power is on.

Log each wafer in a separate file

Two changes were made to accomplish this task. First a counter was setup to track the total number of wafers which pass through the plasma etcher. Each file is stored with the following file heading

#####.rpm

where ##### is a consecutive integer. This counter is stored in a separate file `file_ctr.dat`. This was done in the case of a power outage. We did not want the counter to be initialized each time, but to continue with the last entry recorded.

In order to determine when to close a file and open a new one, corresponding to a new wafer in the system the `rp` variable is once again monitored. When the real power falls below 10 watts, then a delay timer of 45 seconds begins. If this timer elapses then the file is closed and a new file is opened, indicating that processing on the previously wafer has completed and a new one is being loaded into the chamber. Once again, the values used are somewhat arbitrary. The 10 watts limit was chosen as before. The delay timer was chosen, such that we do not terminate the file too soon. Many etch recipes have idle time to allow for stabilization, as previously mentioned, and those delays should not be interpreted that the etch process has been completed for that particular wafer.

Transmission of data files to a local area network of workstations

When the data collection has completed for a particular wafer and all the information has been stored in their prospective files, the files must be transmitted to our network. This is easily accomplished over an ethernet line. The files are automatically sent when data collection begins for the next wafer. The data path used is:

j:\microdat\lam\lam4\#####.rpm

a Different types of text are used to distinguish between program routines, software functions, variables, and text. *Italics* are used for routines in the program, "quotation marks" are used for text or messages, and the helvetica font is used for program variables.

Appendix B

Test Structure Process Steps for the Experiments

The following is the sequence of steps used to fabricate the test structures used in the Lam Rainbow 4400 Experiments.

1. p-type B<100> wafers, 14-22 ohms*cm.
2. Gate ox: Tylan5, 2.5 hours at 950°C. recipe: sgateox (~580A)
3. n+ doped poly: Tylan 11, 3.5 hours recipe: sdopolyh (~6000A)
 - Use the center boat, grow one lot of 12 wafers at a time.
 - Tylan7 anneal 15 min at 950°C.
 - Anneal all 24 wafers together.
4. LTO: Tylan 12, 450C O₂:SiH₄ = 90sccm: 60sccm 16min recipe: vdoltoc (~3000A)
 - Use the rear boat, grow one lot of 12 wafers at a time.
5. Mask 1: Hardbake at least 40 min
 - HMDS 2 - 3 min.
 - Eaton I-line resist, standard process (#15), resist thickness ~0.9um
 - GCA expose mask 1 at standard focus, at exposure dose that can resolve 0.8um elbows. This is generally 31% more than the standard.
 - Post-exposure bake 60 sec. at 120°C
 - MTI develop standard recipe (#70)
 - Technics-C descum for 1 min. at 50W

- Hardbake 20 min. at 120°C
6. Etch LTO: lam2 standard recipe, 750W, 85% endpoint, 30sec. overetch
 7. Etch poly: lam4 standard recipe (Cl_2 : He). Etch to endpoint.
 8. Strip resist: Technics-C, 400W, 7min.
 9. Mask 2: Hardbake at least 40 min.
 - HMDS 2 - 3 min.
 - Eaton I-line resist, standard process (#15), resist thickness ~1.1um
 - GCA expose mask 2 at standard focus, at exposure dose that ca resolve 0.8um elbows
 - Post-exposure bake 60 sec. at 120°C
 - MTI develop standard recipe (#70)
 - Technics-C descum for 1 min. at 50W
 - Hardbake 20 min. at 120°C
 10. Etch LTO: lam2 standard recipe 850W 95% endpoint, 30sec. overetch
 11. Strip resist: Technics-C, 400W, 7min.
 12. Mask 3: Hardbake at least overnight.
 - HMDS 2 - 3 min.
 - Eaton I-line resist, standard process (#15), resist thickness ~1.1um
 - GCA expose mask 3 at standard focus, and at exposure dose that can resolve 0.8um elbows
 - Post-exposure bake 60 sec. at 120°C
 - MTI develop standard recipe (#70)
 - Technics-c descum for 1 min. at 50W
 - Hardbake 30 min. at 120°C